An evaluation of paired $\delta^{18}O$ and $(^{234}U/^{238}U)_0$ in opal as a tool for paleoclimate reconstruction in semi-arid environments

Jessica L. Oster [a,*], Kouki Kitajima [b], John W. Valley [b], Bruce Rogers [c], Katharine Maher [d]

[a] Dept. of Earth and Environmental Sciences, Vanderbilt University, Nashville, TN, United States
[b] WiscSIMS, Dept. of Geoscience, Univ. of Wisconsin, Madison, WI 53706, United States
[c] Western Cave Conservancy, Fremont, CA, United States
[d] Dept. of Geological and Environmental Sciences, Stanford University, CA, United States

ARTICLE INFO

ABSTRACT

Authigenic opal deposits are widespread in semi-arid and arid environments and often contain high uranium concentrations that facilitate high-precision dating by U-series and U-Pb geochronology. However, despite their ubiquity and utility for placing temporal constraints on surficial processes, the potential for authigenic opal deposits to be used as archives of past climate variability remains largely unexplored compared with more frequently used authigenic carbonate deposits. Here we investigate the potential for authigenic opal deposits to provide records of paleoclimate and paleohydrologic variability through the development of a combined record of uranium ($(^{234}U/^{238}U)_0$) and oxygen ($\delta^{18}O$) isotope variability using in situ ion microprobe methods on opal deposits from Pinnacles National Park, California that precipitated from approximately 16 to 3 ka. Pinnacles opal $(^{234}U/^{238}U)_0$ suggests a moderate decrease in net infiltration from the early to middle Holocene, coincident with the timing of increasing aridity inferred from Sierra Nevada lake records, while Pinnacles opal $\delta^{18}O$ indicates a relative increase in subtropical storms at the same time. A shift to more North Pacific sourced storms commenced after ~5 ka coincident with the easing of aridity in Northern California and increased storminess in the Sierra Nevada as indicated by lake sediment records. These results suggest that useful insights about past hydrologic change can be gleaned from authigenic opal deposits, and that these deposits have the potential to enhance the spatial and temporal coverage of paleoclimate reconstructions in regions where other archives might be scarce. However, further study of the influence of water in opal on $\delta^{18}O$ variability and additional in situ analysis of $\delta^{18}O$ variability on longer-lived opal deposits with uniform growth histories are necessary to verify the controls on this potential proxy. Similarly, further investigation into short-term and spatial variability in $(^{234}U/^{238}U)_{sw}$ will improve qualitative and quantitative applications of $(^{234}U/^{238}U)_0$ in authigenic opal deposits, enhancing our ability to use this promising new paleoclimate archive.

1. Introduction

Authigenic minerals, including carbonate and silica deposits, are widespread in semi-arid and arid environments, and can signify past climate and land-surface changes. Dating of these deposits, such as pedogenic clast coatings, vein fillings, and ground water discharge deposits can place chronologic constraints on sediment deposition (e.g. Sharp et al., 2003; Blisniuk et al., 2012; Neymark and Paces, 2013); fault movement (Blisniuk and Sharp, 2003; Nuriel et al., 2012; Robinson et al., 2015) and vadose zone water flow (Neymark et al., 2002; Paces et al., 2010). For minerals precipitated from oxidizing aqueous solutions, U-series and U-Pb dating can provide precise chronologies over thousands to millions of years if samples have high U/Th and U/Pb ratios

and have remained closed to post-depositional mobility of U-series nuclides (e.g., Sharp et al., 2003; Ludwig and Paces, 2002; Maher et al., 2007; Neymark, 2011; Neymark and Paces, 2013; Ibarra et al., 2014).

Authigenic opal deposits are particularly useful for U-series and U-Pb geochronology as they often contain high U concentrations that can permit the use of conventional solution and in situ ion microprobe (Secondary Ion Mass Spectrometry, or SIMS) methods (Paces et al., 2004, 2010; Maher et al., 2007; Neymark, 2011; Neymark and Paces, 2013; Maher et al., 2014). Yet, despite their ubiquity and utility for providing precise temporal constraints on surficial processes, the potential of authigenic opal deposits as archives of past climate variability remains largely unexplored. By comparison, isotopic variations in pedogenic carbonate (e.g. Cerling, 1984; Amundson et al., 1996; Oerter et al., 2016) and clay deposits (Stern et al., 1997; Chamberlain and Poage, 2000; Chamberlain et al., 2012) have provided important records of past changes in plant communities and meteoric water composition related

to climate and tectonic change. The $\delta^{18}O$ variability of carbonate minerals from pedogenic and vadose environments has been analyzed by bulk and microanalytic methods, and has been shown to reflect the $\delta^{18}O$ of precipitation (e.g. Cerling, 1984; Amundson et al., 1996; Oerter et al., 2016), which may reflect air temperature as well as moisture source and transport processes and convective processes (Dansgaard, 1964; Vachon et al., 2010; Aggarwal et al., 2016). However, the analysis of $\delta^{18}O$ variability in authigenic silica is less frequent (Szabo and Kyser, 1990; Alexandre et al., 2004), and ion microprobe work has focused on analyzing quartz (Kelly et al., 2007; Graham et al., 1996) rather than hydrous silica phases. A few studies have investigated the potential for authigenic opal as a climate archive. Variations in U concentration in deep vadose zone opal fracture coatings from Yucca Mountain, Nevada, have been analyzed, and fluctuate on glacial-interglacial timescales (Paces et al., 2010). Likewise, variations in the initial uranium activity ratio $((^{234}U/^{238}U)_0)$ in soil water and soil opal deposits have been shown to reflect changes in net infiltration—precipitation minus evapotranspiration (P-ET) and thus provide a paleoclimate proxy that is sensitive to past changes in rainfall (Oster et al., 2012a; Maher et al., 2014). If authigenic opal deposits can be shown to provide reliable proxy records, even at low temporal resolution, they could fill important spatial gaps in the paleoclimate record due to their widespread occurrence in semi-arid environments, complementing paleoclimate records from archives such as lakes and speleothems (Fig. 1a).

To further explore the potential for authigenic opal deposits to provide records of paleoclimate and paleohydrologic variability, we have developed a combined record of $(^{234}U/^{238}U)_0$ and $\delta^{18}O$ variability using in situ ion microprobe methods on opal coatings precipitated from percolating water on the walls of talus caves within Pinnacles National Park, California. We evaluate these records individually and in relation to the known climate history of this region. Our analysis suggests that records of $\delta^{18}O$ and $(^{234}U/^{238}U)_0$ variability in these materials can provide independent records of the $\delta^{18}O$ of meteoric water, as well as infiltration rate, which is linked to rainfall amount. We therefore suggest that authigenic opal deposits have potential to provide records of paleohydrologic change, and could be of particular importance in regions where other terrestrial paleoclimate archives are scarce. However, further laboratory investigation of the conditions for, and kinetics of, oxygen isotope exchange in amorphous silica, as well as the evaluation of additional coeval, long-lived records from opal deposits with regular growth histories, will improve our ability to use this promising new paleoclimate archive.

2. Materials and methods

2.1. Site and samples

The Pinnacles opal deposit (PNP1) was collected from an active water seep in Balconies Cave, a talus cave formed in rhyolite breccia within Pinnacles National Park (36.4906° N, 121.1825° W) in the Gabilan Range. This location in the central California Coast Range is presently characterized by a Mediterranean climate, with >85% of precipitation occurring during the winter months when the Aleutian Low strengthens and channels winter storms to the region from the Pacific. Pinnacles National Park receives approximately 420 mm of rainfall per year. The $\delta^{18}O$ of modern rainfall shows a significant relationship with moisture source region, with precipitation of high $\delta^{18}O$ associated with enhanced moisture flux from the subtropical and tropical Pacific, and low $\delta^{18}O$ associated with longer traveled storms initiated from the North Pacific (Fig. 1) (Berkelhammer et al., 2012). Subtropical and tropical moisture is often delivered via atmospheric rivers, narrow filaments of concentrated near-surface water vapor that can bring intense rainfall and are associated with flooding along the Pacific coast (Dettinger, 2011). Given the sensitivity to moisture source and its location near the coast in central California, Pinnacles is well situated to document past moisture source changes and, when compared to other
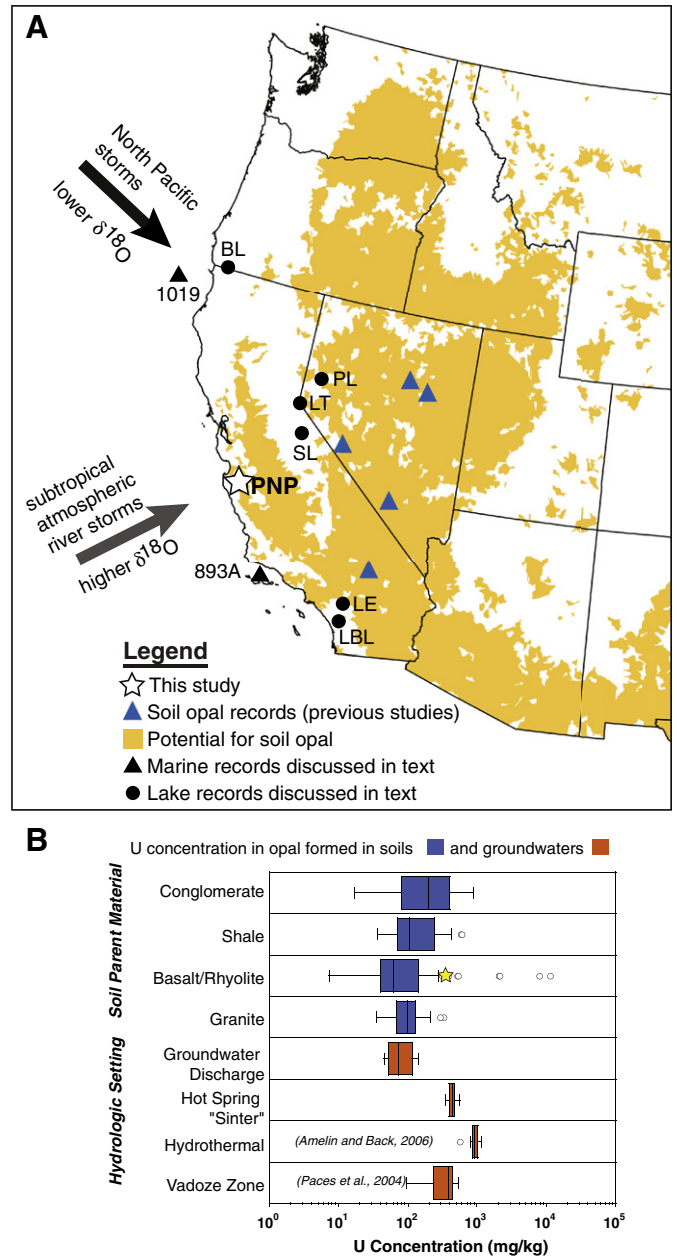

Fig. 1. A) Location of study site (PNP) in central California and sites of other paleoclimate records mentioned in the text: ODP 1019 (Barron et al., 2003); ODP893A (Heusser, 1998); Bolan Lake (BL) (Briles et al., 2005); Pyramid Lake (PL) (Benson et al., 2002; Mensing et al., 2004); Lake Tahoe (LT) (Lindström, 1990; Osleger et al., 2009); Swamp Lake (SL) (Street et al., 2012); Lake Elsinore (LE) and Lower Bear Lake (LBL) (Kirby et al., 2012). Blue triangles show locations of soil and hydrogenic opal analyzed in previous studies (Paces et al., 2010; Maher et al., 2014). Background shading corresponds to potential regions of secondary soil opal/carbonate accumulation based on the arid hydrologic landscape regions defined by Wolock et al. (2004) where precipitation minus potential evapotranspiration is less than −200 mm/year (geospatial data from Wolock, 2003). Large arrows depict idealized storm trajectories reaching PNP. B) Ranges of U concentration in opal deposits from soils (blue boxes) and groundwaters (orange boxes) with parent material and hydrologic setting. Yellow star shows average concentration of U PNP1 opal (77–1975 mg/kg, Table 1). Data from Maher et al., 2014, Amelin and Back, 2006, Paces et al., 2004.

regional records, highlight the variable influences these changes may have had on precipitation amounts in northern versus southern and coastal versus inland locations in western North America.

Balconies Cave consists of a series of passages developed among rhyolite boulders that extend ~25 m below the ground surface. The cave is

overlain by the Highpeaks-Burgundy soil complex, which consists of thin (0 to 25 cm, depending on slope) deposits of gravelly to sandy residuum derived from rhyolite. Vegetation above the cave consists of chaparral species such as chamise and manzanita (USDA, 2007). Opal Hall, where PNP1 was collected, is located beneath ~20 m of rhyolite breccia (Fig. S1). As with regional rainfall, water seepage into Balconies Cave is highly seasonal, ceasing during the dry summer months. Thus, we do not anticipate significant water storage above Balconies Cave, and travel times of water from the surface into Balconies Cave should be <1 year.

PNP1 was sampled from a larger (several 10's of cm^2) coating on the underside of a rhyolite boulder at an active water seep within the Opal Room. Due to its size and presence in an underground void, this precipitation setting differs somewhat from typical pedogenic opal deposits that form as coatings on the undersides of pebbles and cobbles in semi-arid and arid soils (e.g. Maher et al., 2014), but resembles deep vadose zone fractures such as those at Yucca Mountain where opal coatings have been used for paleoclimate study (e.g. Paces et al., 2010), as well as lava tubes that can host opal speleothem precipitation (Hill and Forti, 1997). PNP1 is composed of dense, banded opal interlaminated with calcite (Fig. 2), suggesting that opal was precipitated slowly from a thin film of water, and that opal and calcite precipitation occurred at different time intervals. The precipitation of calcite versus opal may be determined by changes in water chemistry, with opal precipitation being favored as the pH of the precipitating solution is lowered (Hill and Forti, 1997; Woo et al., 2008). To assess coeval opal precipitation, color cathodoluminescence (CL) images were generated by overlaying 3 images collected using red, blue, and green color filters (Fig. 2). CL and backscatter imaging of PNP1 were completed using a Tescan Vega 3 LMU secondary electron microscope with a Gatan MonoCL4 detector at Vanderbilt University.

2.2. Ion microprobe (SHRIMP-RG) ^{230}Th-U analyses and calculation of $(^{234}U/^{238}U)_0$

A ~5 × 5 cm, 2 mm thick section of PNP1 was cut and cross-sections were mounted in epoxy, polished, and examined using optical and scanning electron microscopy to assess stratigraphy, textures, and mineralogy (Fig. 2). ^{230}Th-U ages and $(^{234}U/^{238}U)_0$ values were determined along the growth axis of three separate cross-sections (17-1a, 17-1b, and 22-3) using an approximately 50 μm spot size with the USGS/Stanford SHRIMP-RG (Sensitive High-Resolution Ion Microprobe-Reverse Geometry), a SIMS instrument. We used a primary ion beam of $^{16}O^-$ between 30 and 60 nA and a 100 μm Köhler aperture with no brightness aperture to maximize the beam intensity. Each magnet cycle monitored peaks at masses 224 ($^{28}Si_4^{16}O_7$), 234, 238, 246 ($^{230}Th^{16}O$), 248 ($^{232}Th,^{16}O$), 251 ($^{235}U^{16}O$), and 254 ($^{238}U^{16}O$) following procedures previously applied by Paces et al. (2004), Maher et al. (2007) and Paces et al. (2010). Although the $^{234}U^{16}O$ peak has greater intensity than the metal ^{234}U peak, it is not used because of an unknown interference at approximately 250 amu. The counts at mass 224 were used to normalize to the NIST SRM 611 concentration standard to obtain U concentrations. The majority of the analyses used 12 cycles consisting of 40 second count times per cycle on the ^{234}U peak and 60 s on the $^{230}Th^{16}O$ peak, with 2 second count times on the other isotope peaks. A secular equilibrium opal standard (BZVV, Virgin Valley, NV), originally obtained from the Royal Ontario Museum, was used as an isotope-ratio standard (Paces et al., 2004).

Analytical data and calculated ages are shown in Table 1. We used the program ISOPLOT V.3 (Ludwig, 2003) which uses the half-lives of Cheng et al. (2000) to calculate ages and $(^{234}U/^{238}U)_0$ values according to the following coupled age-dating equations
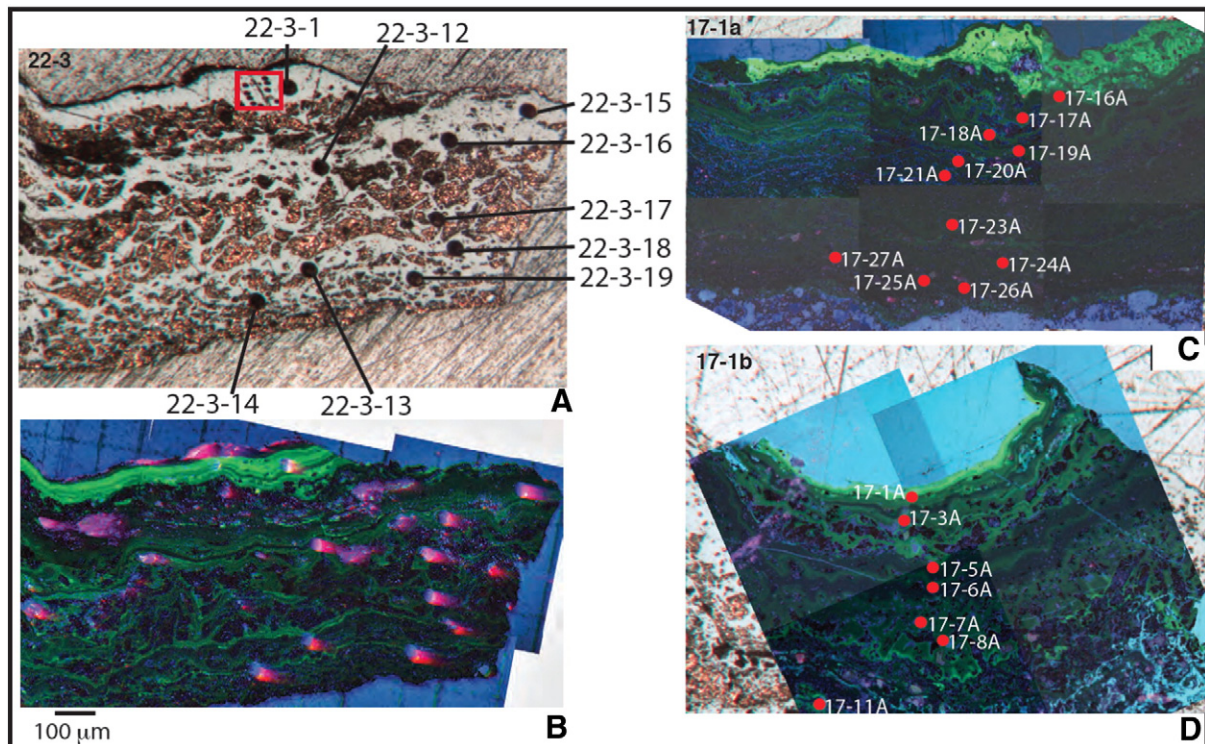
Fig. 2. A) Reflected light image of PNP1 section 22-3. Smooth, white continuous bands are opal. Brown discontinuous bands are calcite. SHRIMP/RG ^{230}Th–-U ages spots are labeled. Values are given in Table 1. Red box outlines δ^{18}O spot analyses along 2 parallel transects shown in Fig. 5. B) Same sample shown in a colour cathodoluminescence image. Opal is bright green and displays banding corresponding to variations in U concentration. Calcite is non-luminescent. Epoxy is blue, and SHRIMP/RG spots are red due to edge effects. C) and D) Same as B for sections 17-1a and 17-1b. Red circles indicate SHRIMP/RG ^{230}Th–-U ages spots, and values are given in Table 1. In general, opal growth proceeded from the bottom to the top of the deposit in each image. Scale bar in B applies to all panels.

Table 1
^{230}Th/U SHRIMP age calculations and initial isotopic data for PNP1. Depths used for building age model are given relative to top of deposit for 17-1a and b and from internal landmarks for 22-3 given concerns over uneven erosion on top of deposit. Points with no given depth were not used in the age model construction for the δ^{18}O time series.

Sample name	Piece	Depth (μm)	(^{230}Th^{16}O/ ^{238}U^{16}O)	±2σ	(^{234}U/^{238}U)	±2σ	(^{230}Th^{16}O/ ^{232}Th^{16}O)	U ppm	Age (ka)	±2σ	(^{234}U/^{238}U)$_0$	±2σ	Age ± 1σ	(^{234}U/^{238}U)$_0$ ± 1σ
17-16A	17-1a	143.1	0.18	0.05	2.04	0.12	6731	129	9.69	2.86	2.07	0.12	1.43	0.06
17-1	17-1a	221.5	0.13	0.02	2.03	0.05	494	1046	7.43	0.90	2.05	0.06	0.45	0.03
17-17A	17-1a	249.2	0.15	0.04	2.01	0.11	4074	138	8.56	2.40	2.03	0.11	1.20	0.06
17-17	17-1a	258.5	0.14	0.02	2.10	0.06	16,638	683	7.37	1.00	2.11	0.06	0.50	0.03
17-16	17-1a	286.2	0.15	0.02	2.15	0.06	20,617	688	7.93	1.02	2.16	0.06	0.51	0.03
17-18A	17-1a	295.4	0.21	0.04	2.07	0.11	6861	174	11.37	2.64	2.10	0.11	1.32	0.05
17-2	17-1a	332.3	0.15	0.02	1.91	0.05	4810	1092	8.74	1.03	1.92	0.05	0.51	0.03
17-19A	17-1a	334.1	0.18	0.04	2.00	0.10	18,510	173	10.46	2.43	2.03	0.10	1.21	0.05
17-21A	17-1a	406.2	0.21	0.06	2.01	0.14	3457	79	11.70	3.64	2.04	0.14	1.82	0.07
17-20A	17-1a	412.6	0.16	0.05	1.98	0.13	2626	93	9.34	3.09	2.01	0.13	1.55	0.07
17-18	17-1a	415.4	0.14	0.02	2.11	0.07	1720	449	7.42	1.14	2.12	0.07	0.57	0.04
17-19	17-1a	480.0	0.17	0.03	2.04	0.09	953	340	9.47	1.64	2.06	0.09	0.82	0.04
17-23A	17-1a	655.4	0.22	0.06	1.99	0.13	6280	170	12.53	3.60	2.03	0.13	1.80	0.07
17-28A	17-1a	710.8	0.20	0.05	2.02	0.12	4627	130	10.98	3.09	2.05	0.13	1.55	0.07
17-27A	17-1a	759.7	0.28	0.07	2.02	0.14	2901	77	15.84	4.40	2.06	0.14	2.20	0.07
17-24A	17-1a	766.2	0.24	0.06	2.02	0.13	5078	114	13.63	3.77	2.06	0.13	1.89	0.07
17-26A	17-1a	816.0	0.26	0.07	1.99	0.15	2416	93	15.25	4.75	2.03	0.16	2.38	0.08
17-25A	17-1a	840.0	0.26	0.08	1.91	0.15	2819	79	15.74	5.12	1.95	0.16	2.56	0.08
17-13	17-1a		0.11	0.01	2.15	0.03	676	1975	5.46	0.38	2.16	0.03	0.19	0.01
17-20	17-1a		0.17	0.03	2.11	0.09	5663	900	9.26	1.78	2.13	0.10	0.89	0.05
17-1A	17-1b	29.5	0.15	0.02	2.00	0.06	427	451	8.14	1.24	2.02	0.06	0.62	0.03
17-3A	17-1b	92.3	0.17	0.04	2.07	0.10	1125	255	9.39	2.26	2.10	0.11	1.13	0.05
17-5A	17-1b	218.5	0.16	0.05	2.04	0.13	7250	102	9.09	2.81	2.07	0.13	1.40	0.06
17-6A	17-1b	275.1	0.17	0.05	2.02	0.12	9501	113	9.57	2.67	2.05	0.12	1.34	0.06
17-7A	17-1b	362.8	0.20	0.05	1.99	0.11	6358	156	11.71	2.84	2.02	0.11	1.42	0.06
17-8A	17-1b	428.3	0.19	0.04	1.94	0.10	7275	188	11.00	2.66	1.97	0.10	1.33	0.05
17-11A	17-1b	590.8	0.21	0.04	1.81	0.08	102	231	13.09	2.50	1.84	0.08	1.25	0.04
17-10A	17-1b	631.4	0.21	0.04	1.90	0.09	124	170	12.64	2.66	1.93	0.09	1.33	0.05
22-3-30A	22-3 bot	73.5	0.16	0.04	2.02	0.12	4586	173	9.09	2.60	2.04	0.12	1.30	0.06
22-3-25A	22-3 bot	104.1	0.17	0.04	1.85	0.10	6867	153	10.42	2.68	1.88	0.10	1.34	0.05
22-3-26A	22-3 bot	187.4	0.17	0.04	1.95	0.10	3054	423	9.78	2.29	1.97	0.10	1.14	0.05
22-3-28A	22-3 bot	196.0	0.22	0.06	1.79	0.14	1859	171	14.02	4.52	1.82	0.14	2.26	0.07
22-3-8	22-3 bot	208.2	0.18	0.02	2.04	0.06	443	213	10.04	1.41	2.07	0.06	0.71	0.03
22-3-27A	22-3 bot	220.5	0.17	0.04	1.99	0.10	1637	187	9.73	2.39	2.02	0.10	1.20	0.05
22-3-29A	22-3 bot	361.3	0.21	0.04	2.02	0.09	1883	291	11.55	2.29	2.06	0.09	1.15	0.05
22-3-3	22-3 mid	31.8	0.12	0.02	2.06	0.05	820	226	6.50	0.92	2.08	0.05	0.46	0.03
22-3-4	22-3 mid	42.9	0.13	0.02	2.09	0.05	2841	181	6.82	1.01	2.11	0.05	0.51	0.03
22-3-15	22-3 mid	46.5	0.17	0.01	2.10	0.04	210	303	8.94	0.82	2.12	0.04	0.41	0.02
22-3-13A	22-3 mid	49.6	0.18	0.05	2.04	0.12	3142	113	9.84	2.83	2.07	0.12	1.41	0.06
22-3-12	22-3 mid	67.3	0.15	0.02	2.11	0.04	1713	256	8.10	0.88	2.14	0.04	0.44	0.02
22-3-14A	22-3 mid	79.6	0.17	0.05	2.05	0.12	9633	165	9.31	2.77	2.08	0.13	1.38	0.06
22-3-5	22-3 mid	85.7	0.14	0.02	2.09	0.06	2957	186	7.70	1.15	2.11	0.06	0.58	0.03
22-3-16	22-3 mid	94.9	0.14	0.02	2.14	0.04	617	222	7.41	0.87	2.16	0.04	0.44	0.02
22-3-15A	22-3 mid	153.1	0.15	0.04	2.06	0.10	4251	181	7.90	2.06	2.08	0.10	1.03	0.05
22-3-18A	22-3 mid	214.3	0.18	0.04	2.03	0.11	2438	165	10.01	2.53	2.06	0.11	1.27	0.05
22-3-19A	22-3 mid	214.3	0.18	0.04	2.02	0.09	589	214	10.01	2.20	2.05	0.10	1.10	0.05
22-3-17	22-3 mid	281.7	0.15	0.02	2.05	0.06	2837	256	8.27	1.21	2.08	0.06	0.61	0.03
22-3-13	22-3 mid	297.6	0.20	0.03	1.97	0.06	1252	126	11.39	1.70	2.00	0.06	0.85	0.03
22-3-18	22-3 mid	355.2	0.19	0.03	2.09	0.08	910	124	10.28	2.00	2.12	0.08	1.00	0.04
22-3-14	22-3 mid	367.4	0.17	0.03	2.04	0.06	1939	202	9.53	1.48	2.07	0.06	0.74	0.03
22-3-19	22-3 mid	400.5	0.17	0.02	1.99	0.05	2435	197	9.77	1.24	2.02	0.05	0.62	0.03
22-3-2A	22-3 top	46.9	0.07	0.01	2.12	0.05	2267	849	3.51	0.65	2.13	0.05	0.33	0.03
22-3-9	22-3 top	53.2	0.05	0.00	2.07	0.02	655	1076	2.70	0.24	2.08	0.02	0.12	0.01
22-3-3A	22-3 top	54.9	0.09	0.02	2.03	0.06	2811	608	4.64	0.90	2.05	0.06	0.45	0.03
22-3-1	22-3 top	57.8	0.06	0.01	2.11	0.03	401	746	3.37	0.32	2.12	0.03	0.16	0.02
22-3-10	22-3 top	79.2	0.07	0.01	2.10	0.03	431	672	3.85	0.35	2.11	0.03	0.18	0.02
22-3-4A	22-3 top	82.6	0.08	0.01	2.12	0.05	775	1069	4.02	0.69	2.14	0.05	0.34	0.02
22-3-2	22-3 top	86.1	0.09	0.01	2.06	0.03	242	683	4.84	0.40	2.07	0.03	0.20	0.02
22-3-12A	22-3		0.11	0.03	2.05	0.10	1169	167	6.13	1.84	2.07	0.10	0.92	0.05
22-3-34A	22-3		0.13	0.04	2.12	0.11	19,250	152	6.82	1.98	2.14	0.11	0.99	0.05
22-3-35A	22-3		0.15	0.04	2.05	0.10	2457	169	8.48	2.10	2.07	0.10	1.05	0.05
22-3-37A	22-3		0.08	0.01	2.02	0.05	855	757	4.23	0.67	2.03	0.05	0.33	0.02
22-3-5A	22-3		0.09	0.01	2.07	0.04	821	966	4.99	0.69	2.08	0.04	0.34	0.02

describing the closed-system decay of ^{234}U and ingrowth and decay of ^{230}Th (assuming no initial ^{230}Th) (Kaufman and Broecker, 1965; Neymark, 2011):

$$\left(\frac{^{234}U}{^{238}U}\right)_t = \left(1 - e^{-\lambda_{234}t}\right) + \left(\frac{^{234}U}{^{238}U}\right)_0 e^{-\lambda_{234}t} \tag{1}$$

$$\left(\frac{^{230}Th}{^{238}U}\right)_t = \frac{\lambda_{230}}{\lambda_{230} - \lambda_{234}} \left(\frac{^{234}U}{^{238}U}\right)_0 \left(e^{-\lambda_{234}t} - e^{-\lambda_{230}t}\right) + \left(1 + \frac{\lambda_{234}e^{-\lambda_{230}t} - \lambda_{230}e^{-\lambda_{234}t}}{\lambda_{230} - \lambda_{234}}\right) \tag{2}$$

where $(^{234}U/^{238}U)_t$ and $(^{230}Th/^{238}U)_t$ are the measured activity ratios, λ_{234} and λ_{230} are the decay constants for ^{234}U and ^{230}Th, respectively.

The equations are solved for $(^{234}U/^{238}U)_0$ and time (t). The measured $^{230}Th^{16}O/^{232}Th^{16}O$ values for each SHRIMP spot are quite high (Table 1), ranging from 100 to 20,600. With such small relative contributions from ^{232}Th, and presumably ^{230}Th, we determined that detrital corrections were insignificant.

The analytical precision on ^{230}Th-U ages and $(^{234}U/^{238}U)_0$ values is typically 5–10% (1 standard deviations, 1 SD) depending on U concentrations and sensitivity. However, even with the large error associated with these in situ analyses, the accuracy is improved in comparison with traditional bulk analytical approaches, which would result in significant age averaging in this finely laminated deposit (Paces et al., 2004; Maher et al., 2007). Additionally, one sample of Pinnacles drip water and one sample of rhyolite host rock were purified by ion exchange chromatography and analyzed for $(^{234}U/^{238}U)$ using a Nu Instruments Plasma HR multi-collector inductively coupled plasma mass spectrometer at Stanford University following procedures outlined in Oster et al. (2012a).

2.3. Ion microprobe $\delta^{18}O$ analyses

Oxygen isotope data and raw $^{16}OH/^{16}O$ ratios were acquired at the Wisconsin Secondary-Ion Mass Spectrometer (SIMS) Laboratory (WiscSIMS) using a CAMECA IMS 1280 large radius multicollector ion microprobe. Oxygen isotope analyses were made along the same three cross-sections as ^{230}Th-U analyses. Prior to isotope analysis, samples were cleaned with deionized water and ethyl alcohol, gold coated, and stored in a vacuum desiccator. For oxygen isotope analyses on the IMS 1280, we used a ~2.1 nA primary beam of $^{133}Cs^+$ ions focused to ~10 μm. Typical intensity of the secondary $^{16}O^-$ beam was 2.5×10^9 cps. Individual analyses lasted approximately 3 min including sputtering of the gold coated surface (10 s), automatic centering of the secondary ion beam in the field aperture using high voltage deflectors (60 s), and 20 cycles of 4 second integrations of oxygen ion measurements. The $^{16}O^-$, $^{16}OH^-$ and $^{18}O^-$ ions were all collected with Faraday cups. Hydride interferences at mass 18 were resolved at Mass Resolving Power (MRP) of 2200, and MRP of ~5000 was used for mass 17 to resolve $^{16}OH^-$ from $^{17}O^-$.

A bulk sample of the BZVV opal standard was measured for $\delta^{18}O$ using a laser fluorination system coupled to a Finnigan MAT 251 mass spectrometer at the University of Wisconsin, Madison Stable Isotope Laboratory. This system employed a special airlock sample chamber to prevent prefluorination of samples (Spicuzza et al., 1998). The average bulk $\delta^{18}O$ of BZVV measured in this way is 23.1 ± 0.6‰ (2 SD, $n = 4$ VSMOW). This value was taken as the true $\delta^{18}O$ value of BZVV and used to calculate the instrumental mass fractionation (IMF) of opal during SIMS analysis. As the IMF of the opal standard was found to be similar to the quartz standard UWQ-1 (IMF = −5.66‰ on average for UWQ-1 versus −5.47 ± 0.8‰, 2 SD, $n = 24$ for BZVV), UWQ-1 was used as the bracketing standard. Four consecutive measurements of UWQ-1 were performed bracketing each set of 10–15 PNP1 sample analyses. The 2 SD precision of a set of bracketing standard analyses on UWQ-1 quartz was used to estimate the spot-to-spot reproducibility of a block of sample measurements (on average 0.33‰). Detailed descriptions of these analytical conditions and the instrument set up have been previously published (Kelly et al., 2007; Page et al., 2007; Kita et al., 2009; Valley and Kita, 2009). Opal $\delta^{18}O$ values are reported relative to Vienna standard mean ocean water (VSMOW). The measured ratios of $^{16}OH/^{16}O$ are used as a measure of the relative water content in each analytical spot, but are not standardized to composition.

2.4. Time-series analysis

We constructed an age model for the $\delta^{18}O$ record with the ^{230}Th-U opal ages and microstratigraphic depth using StalAge (Scholz and Hoffman, 2011), an age modeling algorithm that screens age data for major and minor outliers and inversions and then uses a Monte Carlo

simulation to fit ensembles of straight lines to subsets of age data. Through this procedure, StalAge calculates the age and corresponding 95% confidence limit of each $\delta^{18}O$ measurement. Coeval opal growth layers within the PNP1 cross sections were correlated using color CL imaging (Fig. 2). Bright green banding in CL images is likely due to U concentration variations and traces bands of coeval opal deposition (Paces et al., 2010). Based on BSE and CL imaging of SIMS analysis spots, oxygen isotope sample spots that appeared to incorporate both opal and calcite were excluded from the final analysis. Microstratigraphic depth for $\delta^{18}O$ and ^{230}Th-U spots was determined relative to common landmarks within each cross section. Depths were measured from the center of each spot on the CL images using the measurement tool in Adobe Illustrator, calibrated against the CL image scale bars. For cross sections 17-1a and 17-1b, which are on the same piece of opal crust, the outermost surface of the deposit can be traced between sample transects following CL banding, and thus ^{230}Th-U spots from these cross sections can be reliably placed on the same depth axis. Apparent erosion of the upper surface of piece 22-3 and separation from the rhyolite clast precludes placing these spots on the same depth axis with 17-1a and 17-1b for comparison. However, plots of age versus microstratigraphic depth from landmarks along three sections of 22-3 are provided in Supplementary Fig. S2. Construction of independent age models for all three cross sections permits comparison of $\delta^{18}O$ trends through time between transects.

To facilitate visual comparison between $(^{234}U/^{238}U)_0$ and $\delta^{18}O$ time-series, each was smoothed using a Gaussian kernel density estimation, which is a robust method for comparing irregularly sampled time-series (Rehfeld et al., 2011). We determined the optimal bandwidth (h) for each smoothing function using the Sheather-Jones method (Sheather and Jones, 1991) included in the SiZer package (Sonderegger, 2011) within the statistics program R 2.15.1 (R Core Team, 2012).

3. Results

3.1. $^{230}Th/U$ ages of PNP1

The ^{230}Th-U opal ages of PNP1 indicate a growth interval of 15.8 ± 2.2 to 2.7 ± 0.12 ka (all uncertainties are given as 1 SD, however 2 SD uncertainties are also reported in Table 1), with some possible depositional shifts to calcite. A plot of age versus microstratigraphic depth for 17-1a and 17-1b (Fig. 3) suggests a break in opal deposition occurred between ~490 to 590 μm from the top of the deposit, which translates to approximately 10 to 13 ka. However, calcite U concentrations are not high enough to permit ^{230}Th-U dating by SIMS, so it is not possible to independently verify the timing of calcite precipitation. There is no visible evidence of biogenic precipitation or calcite replacement by opal, and opal ages decrease from the base of the deposit outward (Figs. 3, S2).

3.2. Time series of $\delta^{18}O$ and $(^{234}U/^{238}U)_0$ in PNP1

Age-corrected $(^{234}U/^{238}U)_0$ values for PNP1 vary between 1.82 ± 0.07 and 2.16 ± 0.03 through the course of the record (Table 1). While the PNP1 opal shows overall higher values of $(^{234}U/^{238}U)_0$ than previously measured soil opal deposits due to the different soil parent materials (Oster et al., 2012a), it does display a similar range of $(^{234}U/^{238}U)_0$ variability over this time interval. Between ~10 and 18 ka, soil opal $(^{234}U/^{238}U)_0$ varied from 1.67 ± 0.05 to 1.92 ± 0.07 in Newark Valley, NV, 1.14 ± 0.04 to 1.61 ± 0.1 in Fish Lake Valley, NV, and 1.17 ± 0.04 to 1.26 ± 0.05 in Barstow, CA (Maher et al., 2014). Thus the measured variability in $(^{234}U/^{238}U)_0$ of PNP1 (0.34) falls within the observed range of variability (0.09 to 0.47) at these other sites during the transition from the last glacial period into the Holocene. The $(^{234}U/^{238}U)_0$ values in the PNP1 deposit decrease between 15.7 ± 2.6 and 14.0 ± 2.3 ka, although this decrease is constrained by only three $(^{234}U/^{238}U)_0$ measurements on two cross-sections. The $(^{234}U/^{238}U)_0$ values then increase through the early Holocene to reach a maximum
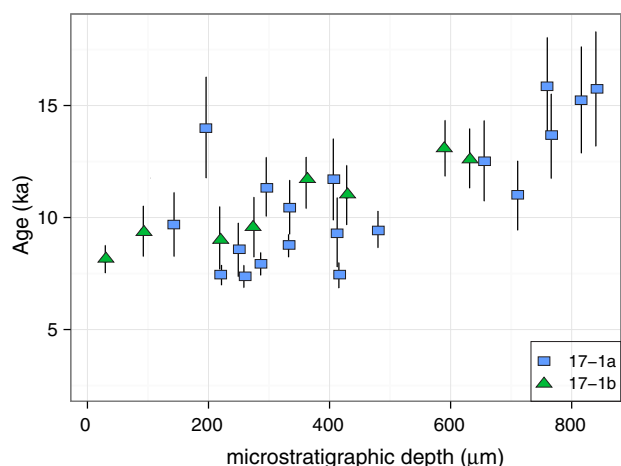
Fig. 3. Plot of age versus microstratigraphic depth from surface of the crust for SHRIMP/RG ^{230}Th–-U ages spots on cross-sections 17-1a and 17-1b.

between ~7 and 6 ka, and remain steady for the remainder of the record (Fig. 4a). All cross-sections of the PNP deposit that were analyzed (17-1a, 17-1b, 22-3) display similar trends (Figs. 4a, S3), demonstrating that $(^{234}U/^{238}U)_0$ is reproducible between coeval layers across the PNP1 opal coating.

Raw and corrected SIMS $\delta^{18}O$ values of PNP1 are given in Table 2. The kernel smoothed value of $\delta^{18}O$ in all cross-sections gradually rises by ~0.75‰ through the early Holocene to reach a maximum at approximately 7 ka, then decreases by the same amount to the end of the record (Fig. 4b). Variability around the mean of 1–1.5‰ is apparent throughout the record, but is especially prevalent in the early-mid Holocene. The same degree of variability is apparent in cross-sections 17-1a and 22-3. Notably, variations in the $\delta^{18}O$ of opal from microstratigraphically correlated opal layers were small and within the analytical precision. This is demonstrated in two parallel traverses of the sample (Figs. 2, 5) that depict overlapping $\delta^{18}O$ trends from ~2–4.5 ka, suggesting little lateral variability in $\delta^{18}O$ in coeval opal over small (~100 μm) lateral distances. However, the degree of variation in the PNP1 $\delta^{18}O$ time series between the analyzed cross-sections (17-1a, 17-1b, 22-3) suggests some variability outside of analytical precision is possible within the coeval portions of the opal crust at larger (100's of microns to cm) lateral scales.

3.3. Evaluating trends in opal $(^{234}U/^{238}U)_0$ and $\delta^{18}O$

Both the opal $(^{234}U/^{238}U)_0$ and $\delta^{18}O$ time-series display some degree of fine-scale variability, although this is particularly evident in the record of opal $\delta^{18}O$ variability. Such variability in pedogenic mineral $\delta^{18}O$ measured using microanalytical techniques is not unprecedented. Analysis of pedogenic carbonates from the Wind River Range in Wyoming similarly found ~1–1.5‰ of scatter around the mean $\delta^{18}O$ values across two pedogenic clast coatings (Oerter et al., 2016). With growth rates of ~0.05 to 0.1 μm/year, this fine-scale variability might reflect real variability in water $\delta^{18}O$ at the annual to centennial scale that is averaged within one 10 μm SIMS pit. This fine-scale variability in opal PNP1 $\delta^{18}O$ values may also be exacerbated by uncertainty on the ^{230}Th/U age model as well as by the small degree of long-term variability in the $\delta^{18}O$ record. Given this fine-scale variability in the data sets, we used the SiZer (SIgnificant ZERo crossings of derivatives) technique to evaluate the significance of trends displayed by both the $(^{234}U/^{238}U)_0$ and $\delta^{18}O$ time-series at a range of temporal scales. SiZer takes smoothing functions calculated across a range of time windows, or bandwidths (h) – shown on the vertical axis of the SiZer plot (Fig. 6) – and classifies the first derivative of each smoothing function along the time series as
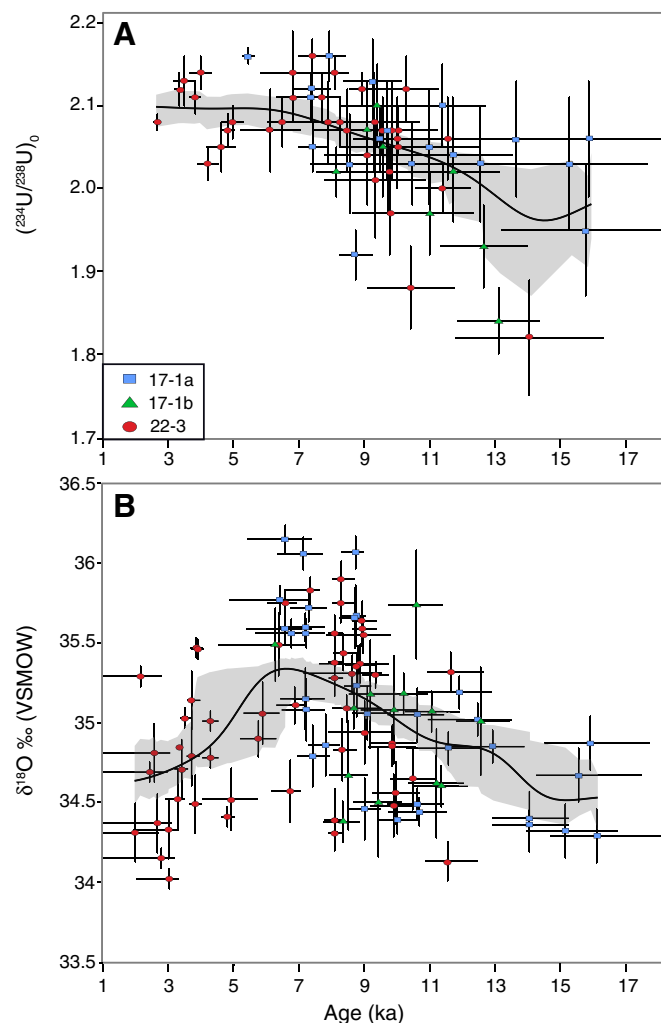
Fig. 4. A) $(^{234}U/^{238}U)_0$ and B) SIMS $\delta^{18}O$ for three cross-sections of PNP1 versus age with associated 1 SD uncertainties. To facilitate visual comparison between $(^{234}U/^{238}U)_0$ and $\delta^{18}O$ records, each was smoothed using a Gaussian kernel density estimation. Gray envelopes are 95% bootstrap confidence intervals calculated using 1000 randomized replicates allowing replacement of individual points using the statistics program R 2.15.1 (R Core Team, 2012).

significantly increasing (red), significantly decreasing (blue), or possibly zero (purple) (Chaudhuri and Marron, 1999). In other words, SiZer can account for the influence of fine-scale variability in the dataset and determine the significance of increasing or decreasing trends at wider or narrower smoothing windows, allowing inclusion of more or fewer data points (larger or smaller slices of time) in the calculation of the smoothing function. Moving from bottom to top on the SiZER plots (Fig. 6), colors define trends that manifest on increasingly longer timescales. The white lines on the diagrams give a graphical representation of the bandwidth, with the distance between the two lines being equal to 2 h. The SiZer analysis of the PNP1 record suggests that the trends apparent in both the $(^{234}U/^{238}U)_0$ and $\delta^{18}O$ datasets at the bandwidth used for the kernel smoothing functions are significant across multiple bandwidths (Fig. 6). A significant ($p = 0.05$) increase in $(^{234}U/^{238}U)_0$ is observed across all examined bandwidths between 8 and 12 ka. A significant increase in $\delta^{18}O$ between ~8.5 and 10 ka is observed at all bandwidths and this significant increase begins earlier in the Holocene with progressively larger bandwidths. The smoothed opal $\delta^{18}O$ record reaches a maximum around ~7 ka (Fig. 4b), and in the SiZer analysis, this is marked by a purple, or flat trend between 6 and 8 ka. A significant decrease in $\delta^{18}O$ is observed at all bandwidths between ~4.2 and 6 ka. This analysis indicates that, despite the fine-scale

Table 2

Ion microprobe (raw and corrected) oxygen isotope values, OH/O values, depths, and model ages for PNP1. As with Table 1, depths used for building age model are given relative to top of deposit for 17-1a and b and from internal landmarks for 22-3 given concerns over uneven erosion on top of deposit.

Sample name	Depth (μm)	δ^{18}O ‰ VSMOW	Error 2SD	IMF ‰	δ^{18}O ‰ raw	Error 2SE	Age model (ka)	Age + error (ka)	Age-error (ka)	δ^{18}O error 1SD	^{16}OH/^{16}O
17-1a											
17-1-1	28.6	35.77	0.18		29.912	0.220	6.43	8.23	3.28	0.09	2.94E-03
17-1-2	65.5	36.15	0.18		30.290	0.236	6.59	8.23	4.26	0.09	3.50E-03
17-1-3	86.8	35.56	0.18		29.703	0.201	6.77	8.25	4.57	0.09	3.57E-03
17-1-4	166.2	35.60	0.18		29.740	0.189	7.20	8.38	5.65	0.09	3.46E-03
17-1-5	193.9	35.56	0.18		29.702	0.184	7.22	8.38	5.65	0.09	3.56E-03
17-1-6	212.3	35.72	0.18		29.864	0.263	7.31	8.43	6.17	0.09	3.42E-03
17-1-8	535.4	34.39	0.18		28.537	0.183	10.02	11.35	8.81	0.09	3.42E-03
17-1-9	576.0	34.44	0.18		28.583	0.241	10.69	12.38	8.81	0.09	3.48E-03
Bracket UWQ-1		12.33		−5.66	6.602	0.18					
17-1-11	652.6	35.19	0.21		29.303	0.186	11.92	13.95	9.41	0.10	3.51E-03
17-1-12	572.3	34.49	0.21		28.607	0.156	10.63	12.29	8.81	0.10	3.52E-03
17-1-13	692.3	35.02	0.21		29.140	0.133	12.49	14.55	9.41	0.10	3.57E-03
17-1-14	720.0	34.85	0.21		28.964	0.224	12.95	14.88	10.37	0.10	3.38E-03
17-1-17	64.6	35.59	0.21		29.706	0.175	6.58	8.23	4.23	0.10	2.91E-03
17-1-18	133.9	36.06	0.21		30.168	0.181	7.13	8.34	5.54	0.10	3.49E-03
17-1-19	336.9	36.07	0.21		30.185	0.189	8.75	9.25	7.88	0.10	3.48E-03
17-1-20	632.3	34.84	0.21		28.955	0.182	11.58	13.55	9.00	0.10	3.52E-03
Bracket UWQ-1		12.33		−5.68	6.576	0.21					
17-1-21	766.2	34.40	0.34		28.632	0.215	14.07	16.49	11.81	0.17	3.45E-03
17-1-22	858.5	34.29	0.34		28.526	0.182	16.14	20.20	13.27	0.17	3.31E-03
17-1-24	830.8	34.67	0.34		28.900	0.264	15.58	19.43	12.96	0.17	3.51E-03
17-1-25	849.3	34.87	0.34		29.103	0.241	15.93	19.59	13.13	0.17	3.45E-03
17-1-26	812.3	34.32	0.34		28.551	0.200	15.16	18.40	12.81	0.17	3.30E-03
17-1-27	766.2	34.36	0.34		28.597	0.260	14.07	16.49	11.81	0.17	4.60E-03
17-1-29	572.3	35.05	0.34		29.283	0.144	10.63	12.29	8.81	0.17	3.53E-03
17-1-30	480.0	35.06	0.34		29.289	0.190	9.10	10.54	8.17	0.17	3.69E-03
Bracket UWQ-1		12.33		−5.57	6.687	0.34					
17-1-31	452.3	34.46	0.39		28.64	0.20	9.02	10.02	7.99	0.19	3.22E-03
17-1-32	374.8	35.23	0.39		29.41	0.23	8.78	9.62	7.99	0.19	3.45E-03
17-1-33	252.0	34.86	0.39		29.03	0.20	7.82	8.68	6.74	0.19	3.45E-03
17-1-34	343.4	35.67	0.39		29.84	0.25	8.75	9.34	7.88	0.19	3.48E-03
17-1-35	321.2	35.66	0.39		29.83	0.16	8.73	9.12	7.76	0.19	3.49E-03
17-1-38	198.5	35.08	0.39		29.26	0.20	7.22	8.39	5.73	0.19	3.41E-03
17-1-39	154.2	35.15	0.39		29.33	0.25	7.20	8.38	5.65	0.19	3.45E-03
17-1-40	221.5	34.79	0.39		28.97	0.18	7.43	8.48	6.46	0.19	3.48E-03
Bracket UWQ-1		12.33		−5.63	6.634	0.39					
17-1b											
17-1-41	30.5	34.38	0.26		28.418	0.239	8.35	9.41	7.18	0.13	3.04E-03
17-1-42	68.3	35.09	0.26		29.117	0.205	8.69	10.38	7.32	0.13	3.28E-03
17-1-43	268.6	35.18	0.26		29.207	0.299	10.21	11.70	8.34	0.13	3.38E-03
17-1-44	373.9	35.07	0.26		29.098	0.162	11.07	12.76	9.43	0.13	3.26E-03
17-1-45	418.2	34.60	0.26		28.633	0.175	11.37	13.00	9.70	0.13	3.26E-03
Bracket UWQ-1		12.33		−5.77	6.493	0.26					
17-1-46	565.9	35.01	0.68		29.286	0.208	12.58	14.32	11.06	0.34	3.59E-03
17-1-50	49.8	34.67	0.68		28.948	0.220	8.52	9.71	7.32	0.34	3.04E-03
17-1 51	129.2	35.18	0.68		29.458	0.219	9.19	10.65	7.87	0.34	3.25E-03
17-1 52	161.5	34.50	0.68		28.780	0.266	9.44	10.84	7.87	0.34	3.47E-03
17-1 53	228.0	35.08	0.68		29.360	0.172	9.91	11.41	7.89	0.34	3.17E-03
17-1 54	317.5	35.74	0.68		30.011	0.197	10.60	12.22	8.89	0.34	3.30E-03
17-1 55	395.1	34.62	0.68		28.905	0.214	11.22	12.91	9.53	0.34	3.27E-03
Bracket UWQ-1		12.33		−5.53	6.735	0.68					
17-1-56	15.7	35.49	0.46		29.562	0.222	6.28	8.23	2.81	0.23	2.80E-03
Bracket UWQ-1		12.33		−5.72	6.537	0.46					
22-3											
22-3 1 top	12.5	34.31	0.37		29.046	0.249	1.98	3.44	−7.25	0.18	2.85E-03
22-3 2 top	33.3	34.37	0.37		29.110	0.232	2.66	3.57	−1.80	0.18	2.90E-03
22-3 3 top	30.8	34.81	0.37		29.542	0.256	2.57	3.55	−2.46	0.18	3.03E-03
22-3 4 top	43.7	34.33	0.37		29.068	0.180	3.01	3.64	0.86	0.18	2.98E-03
22-3 5 top	54.7	34.71	0.37		29.444	0.142	3.41	3.81	2.96	0.18	3.05E-03
22-3 6 top	71.2	34.49	0.37		29.223	0.250	3.82	4.26	3.47	0.18	2.98E-03
22-3 7 top	51.6	34.52	0.37		29.261	0.239	3.29	3.73	2.52	0.18	2.94E-03
22-3 8 top	66.3	35.14	0.37		29.869	0.220	3.72	4.24	3.42	0.18	3.02E-03
22-3 9 top	65.7	34.79	0.37		29.526	0.204	3.71	4.21	3.41	0.18	3.00E-03
Bracket UWQ-1		12.33		−5.09	7.179	0.37					
22-3-11 mid	13.8	34.52	0.39		29.240	0.231	4.92	6.53	3.15	0.20	2.97E-03
22-3-12 mid	24.5	35.06	0.39		29.784	0.109	5.89	6.93	4.72	0.20	2.83E-03
22-3-13 mid	91.2	34.39	0.39		29.111	0.164	8.10	8.62	7.73	0.20	3.01E-03
22-3-14 mid	137.8	34.83	0.39		29.548	0.199	8.33	9.21	7.77	0.20	2.73E-03
22-3-15 bot	49.0	34.94	0.39		29.662	0.158	9.02	10.67	6.77	0.20	2.94E-03
22-3-16 bot	125.5	34.48	0.39		29.202	0.225	9.91	11.39	8.49	0.20	2.93E-03
22-3-17 bot	132.3	34.56	0.39		29.288	0.304	9.97	11.45	8.52	0.20	2.97E-03

Table 2 (continued)

Sample name	Depth (μm)	$\delta^{18}O$ ‰ VSMOW	Error 2SD	IMF ‰	$\delta^{18}O$ ‰ raw	Error 2SE	Age model (ka)	Age + error (ka)	Age-error (ka)	$\delta^{18}O$ error 1SD	$^{16}OH/^{16}O$
22-3-18 bot	189.8	34.65	0.39		29.373	0.195	10.49	11.84	9.08	0.20	2.88E-03
22-3-19 mid	30.6	35.49	0.39		30.210	0.197	6.39	7.16	5.30	0.20	2.91E-03
22-3-20 mid	33.7	34.57	0.39		29.293	0.177	6.74	7.39	5.59	0.20	3.09E-03
Bracket UWQ-1		12.33		−5.1	7.167	0.39					
22-3-21 mid	22.7	34.90	0.23		29.454	0.233	5.76	6.86	4.63	0.11	2.91E-03
22-3-25 mid	79.6	35.56	0.23		30.109	0.213	8.10	8.62	7.73	0.11	2.88E-03
22-3-26 mid	134.7	35.90	0.23		30.444	0.230	8.30	9.15	7.77	0.11	3.03E-03
Bracket UWQ-1		12.33		−5.26	7.002	0.23					
22-3-31 mid	34.9	35.11	0.23		29.633	0.210	6.88	7.46	5.73	0.12	2.97E-03
22-3-32 mid	64.3	35.28	0.23		29.801	0.194	8.10	8.62	7.72	0.12	2.92E-03
22-3-33 mid	91.9	35.38	0.23		29.901	0.228	8.10	8.62	7.73	0.12	2.91E-03
22-3-35 mid	140.8	35.44	0.23		29.961	0.202	8.36	9.26	7.78	0.12	2.99E-03
22-3-36 mid	183.7	35.59	0.23		30.111	0.235	8.94	9.83	8.30	0.12	2.93E-03
22-3-38 bot	12.2	35.31	0.23		29.831	0.222	8.63	10.48	5.66	0.12	2.89E-03
22-3-39 bot	45.9	35.55	0.23		30.067	0.171	8.98	10.65	6.68	0.12	2.91E-03
22-3-40 bot	122.5	34.87	0.23		29.390	0.202	9.87	11.34	8.42	0.12	3.00E-03
Bracket UWQ-1		12.33		−5.29	6.971	0.23					
22-3-41 bot	121.2	34.85	0.25		29.442	0.163	9.86	11.31	8.39	0.12	3.02E-03
22-3-42 bot	34.9	35.37	0.25		29.962	0.202	8.88	10.62	6.36	0.12	2.97E-03
22-3-43 bot	165.3	33.73	0.25		28.329	0.189	10.27	11.82	8.52	0.12	
22-3-45 bot	367.4	35.32	0.25		29.914	0.179	11.66	13.71	10.23	0.12	2.91E-03
22-3-46 bot	355.2	34.13	0.25		28.732	0.206	11.56	13.41	10.18	0.12	3.03E-03
22-3-47 mid	189.8	35.36	0.25		29.957	0.233	8.80	9.83	8.01	0.12	2.92E-03
22-3-48 mid	232.7	35.64	0.25		30.235	0.176	8.94	9.83	8.30	0.12	3.01E-03
22-3-50 mid	108.4	35.75	0.25		30.344	0.190	8.29	9.14	7.76	0.12	2.98E-03
Bracket UWQ-1		12.33		−5.22	7.044	0.25					
22-3 51 top	86.5	34.41	0.13		29.089	0.213	4.81	5.27	4.42	0.06	2.87E-03
22-3 52 top	17.9	35.29	0.13		29.958	0.163	2.15	3.48	−5.75	0.06	3.05E-03
22-3 53 top	26.5	34.69	0.13		29.370	0.213	2.43	3.53	−3.51	0.06	2.90E-03
22-3 54 top	44.3	34.02	0.13		28.700	0.207	3.03	3.64	1.02	0.06	2.92E-03
22-3 55 top	36.9	34.15	0.13		28.829	0.209	2.78	3.60	−0.85	0.06	2.81E-03
22-3 56 top	57.8	35.03	0.13		29.701	0.248	3.50	3.85	3.20	0.06	2.90E-03
22-3 57 top	73.1	35.47	0.13		30.143	0.306	3.86	4.26	3.48	0.06	3.00E-03
22-3 58 top	84.4	35.01	0.13		29.683	0.238	4.29	4.78	3.78	0.06	2.90E-03
22-3 59 top	84.4	34.78	0.13		29.453	0.219	4.29	4.78	3.78	0.06	2.83E-03
22-3 60 top	76.2	35.46	0.13		30.132	0.209	3.90	4.26	3.48	0.06	3.00E-03
Bracket UWQ-1		12.33		−5.15	7.120	0.13					
22-3-61 mid	39.8	35.83	0.17		30.424	0.186	7.35	7.92	5.73	0.08	2.98E-03
22-3-62 mid	45.9	34.31	0.17		28.910	0.143	8.10	8.62	7.45	0.08	3.01E-03
22-3-63 mid	32.5	35.75	0.17		30.346	0.167	6.59	7.30	5.47	0.08	2.90E-03
22-3-64 mid	153.1	35.09	0.17		29.690	0.212	8.47	9.50	7.82	0.08	2.98E-03
22-3-65 mid	275.6	35.30	0.17		29.893	0.243	9.35	10.16	8.53	0.08	3.07E-03
Bracket UWQ-1		12.33		−5.22	7.045	0.17					
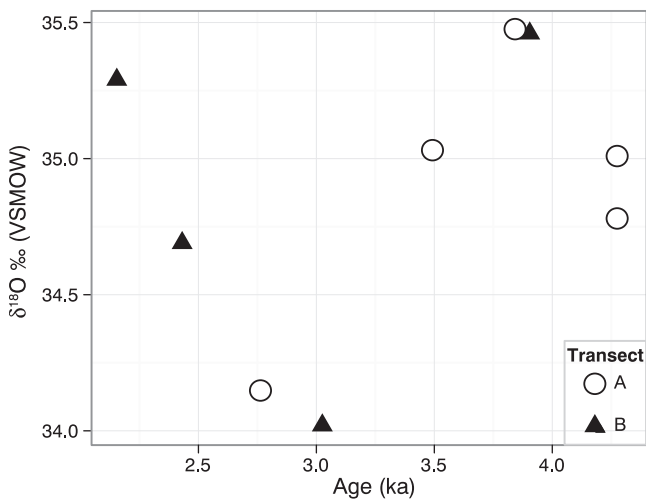
Fig. 5. $\delta^{18}O$ for two parallel transects in cross section 22-3 (red box, Fig. 2a, Transect A on left, Transect B on right). CL banding was used to identify coeval material. Transects show similar trends and coeval points overlap within analytical uncertainty (on average 0.33‰).

variability in these datasets, the long-term trends described by the kernel smoothing functions are consistent across a wide range of smoothing windows. The slight decrease in $(^{234}U/^{238}U)_0$ between 14 and 15 ka that is apparent in the kernel smoothing function (Fig. 4a) is not found to be significant by the SiZer analysis. Likely this is due to the relative sparseness of the data set during this interval. Unfortunately, data collection becomes more challenging in the older part of the PNP1 opal deposit due to the large 50 μm spot size used for ^{230}Th-U analysis that could lead to incorporation of the rhyolite host rock in the analysis of the oldest opal material. Thus more reliable ^{230}Th-U analyses of older material were difficult to obtain.

4. Discussion

The PNP1 opal deposit displays measureable shifts in both $(^{234}U/^{238}U)_0$ and $\delta^{18}O$ across its depositional history during the Holocene. However, both records, particularly the $\delta^{18}O$ record, display a noticeable degree of fine-scale variability. In the following section, we discuss potential drivers of long-term variability in both parameters, including environmental influences and what the observed shifts in $(^{234}U/^{238}U)_0$ and $\delta^{18}O$ may suggest from a paleoclimate standpoint. We also describe factors that could contribute to uncertainty in interpreting opal $(^{234}U/^{238}U)_0$ and $\delta^{18}O$ as paleoclimate proxies and potential future steps toward mitigating this uncertainty.
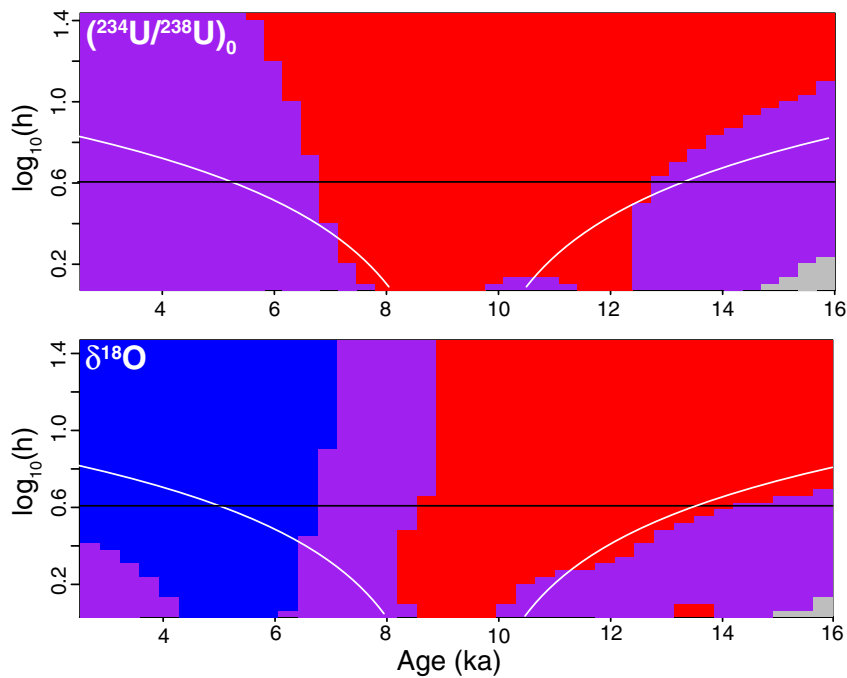
Fig. 6. SiZer Map for the uranium (upper panel) and oxygen (lower panel) isotope time-series for the PNP1 sample with time on the x-axes. Y-axes show the log of bandwidths (h) examined for the smoothing function. Horizontal black lines at 0.6 denote the bandwidth used for kernel smoothing function for the $(^{234}U/^{238}U)_0$ and $\delta^{18}O$ time-series shown in Fig. 4. Red shading denotes periods where the data display increasing trends at a given bandwidth, blue denotes periods of decreasing trends, and purple denotes periods of no or insignificant trends. Moving from bottom to top, colors define trends that manifest on increasingly longer timescales. The white lines give a graphical representation of the bandwidth, with the distance between the two lines being equal to 2 h.

4.1. Opal $(^{234}U/^{238}U)_0$ as a paleoclimate signal

The most abundant isotope of natural uranium is ^{238}U, which decays through two short-lived daughter products (^{234}Th and ^{234}Pa) to radioactive ^{234}U. In rocks older than ~1 million years, this system should be at secular equilibrium, where the activity ratio of $(^{234}U/^{238}U)$ is equal to one. However, groundwaters and surface waters generally are not in secular equilibrium, and often have $(^{234}U/^{238}U)$ values greater than one (Riotte and Chabaux, 1999; Porcelli and Swarzenski, 2003; Robinson et al., 2004). This enrichment in ^{234}U over ^{238}U is generally attributed to the α-recoil of the daughter isotope that occurs when ^{238}U decays to ^{234}Th. The recoil distance for ^{234}Th is approximately 30 to 50 nm in silicate minerals (Kigoshi, 1971; Maher et al., 2006). As a result, ^{234}Th can be directly ejected into seepage waters where it quickly decays to ^{234}U, or if it remains within the mineral grain, the resulting ^{234}U can be removed by preferential leaching from damaged recoil tracks (Kigoshi, 1971; Andersen et al., 2009). Thus, the $(^{234}U/^{238}U)$ of seepage waters, and $(^{234}U/^{238}U)_0$ of secondary minerals, should reflect a balance between two processes: α-recoil, that will increase $(^{234}U/^{238}U)$, and congruent dissolution of minerals at or near secular equilibrium, that will tend to decrease it (Maher et al., 2006; Oster et al., 2012a).

Based on studies of modern $(^{234}U/^{238}U)$ in soil waters (defined here as $(^{234}U/^{238}U)_{sw}$ Table 3), as dilute rainfall infiltrates into the soil, the $(^{234}U/^{238}U)_{sw}$ increases along the flowpath as more α-recoil-derived ^{234}U is gradually added to the fluid (Paces et al., 2002; Maher et al., 2006; Bourdon et al., 2009; Oster et al., 2012a; Schaffhauser et al., 2014). This enrichment in ^{234}U is balanced by the weathering of the bulk solids. Higher infiltration fluxes allow less time for ^{234}U to accumulate, resulting in lower $(^{234}U/^{238}U)_{sw}$ values at a given depth. Chemical weathering rates also increase with increasing water flux, which results in greater amounts of congruent dissolution and further reduction of the fluid $(^{234}U/^{238}U)_{sw}$. Changes in the water flux can thus be directly related to the measured $(^{234}U/^{238}U)_0$ of secondary minerals assuming that other parameters like mineralogy and particle size in soils remained constant. An advantage of $(^{234}U/^{238}U)_0$ in authigenic minerals

over light, stable isotope systems such as $\delta^{18}O$ is that there is negligible uranium isotope fractionation during carbonate precipitation or evaporation, so secondary minerals should directly reflect the water from which they grew. Variations in $(^{234}U/^{238}U)_0$ in pedogenic carbonates as well as speleothems and lacustrine carbonates have previously been used as qualitative indicators of infiltration, and thus rainfall variability, in conjunction with other proxy records (Ayalon et al., 1999; Hellstrom and McCulloch, 2000; Frumkin and Stein, 2004; Polyak et al., 2012; McGee et al., 2012; Oerter et al., 2016).

4.1.1. $(^{234}U/^{238}U)_0$-based model of infiltration and precipitation for PNP

The $(^{234}U/^{238}U)_0$ of PNP1 increased by 0.14 (kernel smoothed data) to 0.34 (full range of variability) across the early to middle Holocene, which suggests a general decrease in infiltration rate during this time. To determine whether the range of $(^{234}U/^{238}U)_0$ represents a reasonable shift in infiltration rates (P-ET), we used an advection-reaction model to place these changes in $(^{234}U/^{238}U)_0$ in a quantitative context and to compare to previous studies of pedogenic opal. The $(^{234}U/^{238}U)_{sw}$ at isotopic steady state is expressed as (Maher et al., 2014):

$$A_{sw} = A_s + \frac{\lambda_{234} F_\alpha}{10^{-2.3}[1 - \exp(-0.01q)]} \qquad (3)$$

Table 3
Abbreviations used in text and equations.

Parameter	Description	Units (or values)
A_s	$(^{234}U/^{238}U)$ in weathering solids	
A_{sw}	$(^{234}U/^{238}U)$ in soil water (also $(^{234}U/^{238}U)_{sw}$)	
F_α	Alpha recoil loss factor	
λ_{234}	Decay constant for ^{234}U	
		2.83×10^{-6} year^{-1}
$\delta^{18}O_{precip}$	$\delta^{18}O$ of precipitation	
q	net infiltration, P-ET	m/year
$(^{234}U/^{238}U)_{sw}$	$(^{234}U/^{238}U)$ in soil water	
$(^{234}U/^{238}U)_0$	initial $(^{234}U/^{238}U)$ in secondary minerals	

where A_{sw} is $(^{234}U/^{238}U)_{sw}$, A_s is the U isotopic ratio of the weathering solids, λ_{234} is the decay constant for ^{234}U (2.83×10^{-6}), q is net infiltration, which is assumed to equal P-ET, and F_α is the α-recoil loss factor, or the fraction of ^{238}U decays that ultimately result in ^{234}U loss from the solid (see Table 3 for a list of abbreviations). The denominator in Eq. (3) is the dissolution rate of the solids, which is related to the infiltration flux through a relationship determined by evaluation of weathering rates across a range of soil ages and climate regimes (Maher, 2010). For higher values of q, or faster infiltration rates, weathering dominates, and A_{sw} will approach the $(^{234}U/^{238}U)$ of the dissolving solids (A_s), which is typically close to one. For lower values of q, α-recoil will dominate, and A_{sw} will increase. Solving Eq. (3) for q, gives P-ET corresponding to the measured $(^{234}U/^{238}U)_{sw}$ or A_{sw}.

$$q = -100 \ln\left(1 - \frac{\lambda_{234} F_\alpha}{10^{-2.3}(A_{sw} - A_s)}\right) \tag{4}$$

To model the PNP system, we set A_s equal to the measured value for PNP rhyolite host rock (0.9936 ± 0.0028). For F_α we used a value of 0.1, which is within the range of F_α measured for soils developed in granitic and rhyolitic parent materials in Fish Lake Valley, NV (Oster et al., 2012a).

Using Eq. (4) and the measured $(^{234}U/^{238}U)_{sw}$ of modern PNP drip water (average value of 2.122 ± 0.006 (2 SD)), we calculate a present infiltration rate of 5 mm/year, which we interpret to be reasonable for this area that receives ~420 mm/year of precipitation. By comparison, the modern infiltration rate estimated using a power law relationship between precipitation and infiltration for Fish Lake Valley, Nevada, which receives ~120–180 mm/year precipitation depending on elevation, is $2.3 + 1.2/-0.9$ mm/year (Maher et al., 2014). For measured PNP1 $(^{234}U/^{238}U)_0$ values, we calculate an initial increase in P-ET of $8.5 \pm 6.5\%$ between 15.7 ± 2.6 and 14.0 ± 2.3 ka. This range encompasses a minimum estimate from the kernel density estimation up to the full range of measured $(^{234}U/^{238}U)_0$ variability. As noted previously, the low density of data in this time period limits our interpretation of P-ET changes in this interval. Model results indicate a decrease in P-ET of $21 \pm 9\%$ between 14.0 ± 2.3 and 6.5 ± 0.5 ka.

In this model scenario, the only variable that is not directly constrained by measurement in the PNP system is the F_α parameter. This parameter is closely related to grain size of the weathering solids. If grain size is small there is greater likelihood that ^{238}U atoms will be located close to a grain boundary and ^{234}Th will be ejected into the pore fluid during α-decay (Neymark, 2011). Decreases in F_α will lead to generally lower $(^{234}U/^{238}U)_{sw}$ values and also somewhat reduced sensitivity of the model to changes in absolute infiltration rate (Fig. 7). For instance, for a smaller F_α of 0.07, the measured $(^{234}U/^{238}U)_{sw}$ for PNP of 2.12 ± 0.006 (2 SD) will yield a q of 3.5 mm/year, and the range of estimates of q derived from the kernel smoothed $(^{234}U/^{238}U)_0$ is 3.5 to 4.0 mm/year compared to a range of 5.1 to 5.8 mm/year for an F_α of 0.1 (Fig. 9). However, in terms of the relative difference, or % change, in q across the range of measured $(^{234}U/^{238}U)_0$, the effect of varying the F_α parameter is negligible, and thus we refer to the relative changes in q in this study.

4.2. Additional drivers for $(^{234}U/^{238}U)_0$ variability and potential future steps

Apparent variations in primary $(^{234}U/^{238}U)_0$ can also arise from open system behavior when U and ^{230}Th exchange with fluids after initial opal deposition (Neymark, 2011). As U is more mobile than Th under oxic conditions, open system behavior tends to result in increased $(^{234}U/^{238}U)_0$ with calculated age. For PNP1, older opal tends to display lower $(^{234}U/^{238}U)_0$ values and temporal variations in $(^{234}U/^{238}U)_0$ are also reproduced on all three measured cross sections (Fig. 4a). In addition, due to high U concentrations, opal is less sensitive to small amounts of open system exchange than is carbonate (Neymark, 2011).
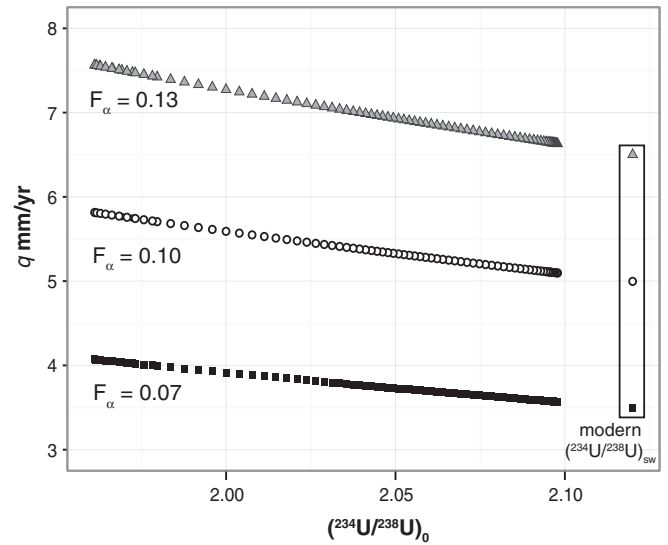
Fig. 7. Modeled infiltration rates (q) given in mm/year for values of $(^{234}U/^{238}U)_0$ taken from the kernel smoothed PNP1 record calculated using Eq. (4). Three different values for F_α are used in the model (0.07, 0.10, 0.13). Calculated values for q based on modern PNP seepage water for each value of F_α are highlighted by the black rectangle. Absolute values and range of variability for q increases with increasing F_α, but the relative change in q across the range of measured $(^{234}U/^{238}U)_0$ is the same for all three scenarios.

Thus, although the influence of open-system exchange on ages and $(^{234}U/^{238}U)_0$ of PNP1 cannot be entirely ruled out, we assume that in the uranium-rich PNP1 opal, variations in $(^{234}U/^{238}U)_0$ are driven by changes in the $(^{234}U/^{238}U)_{sw}$ from which the opal originally precipitated due to changes in infiltration rates (Maher et al., 2014; Oster et al., 2012a). However, given the potential for open-system behavior to influence $(^{234}U/^{238}U)_0$ records, additional dating methods, such as the $^{231}Pa/^{235}U$ system (Edwards et al., 1997) or ^{14}C in carbonates (Ibarra et al., 2014), could be used to check for concordance in ages, and thus to increase confidence in the interpretation of environmental signals associated with $(^{234}U/^{238}U)_0$. Such alternative dating methods are not approachable by SIMS and would require larger samples.

Closer investigations of the processes that result in $(^{234}U/^{238}U)_0$ variability at fine spatial scales within hydrogenic deposits could also improve the use of U isotopes as a qualitative or quantitative tool for paleoclimate studies. Given the known dependence of $(^{234}U/^{238}U)_{sw}$ on hydrologic processes (Bourdon et al., 2009; Hubert et al., 2006; Maher et al., 2006; Oster et al., 2012a), which can vary widely over synoptic, seasonal and decadal timescales, high-frequency temporal variability may influence $(^{234}U/^{238}U)_0$ in both rapidly growing material or slow growing material measured at high spatial resolution. Although the ability of $(^{234}U/^{238}U)$ to trace source mixing relationships in ground waters and rivers has been demonstrated (e.g. Chabaux et al., 2001; Durand et al., 2005; Kraemer and Brabets, 2012; Paces and Wurster, 2014), additional studies of the variability of soil water and groundwater $(^{234}U/^{238}U)$ on short timescales and its underlying causes are necessary to improve the use of this promising tool. Furthermore, additional investigations of $(^{234}U/^{238}U)_{sw}$ in karst environments (e.g. Kaufman et al., 1998; Zhou et al., 2005; Guerrero et al., 2016), including talus caves like PNP, would assist in determining the applicability of the infiltration model presented above in these settings as well as any influence of spatial heterogeneity in flow paths on recorded $(^{234}U/^{238}U)_0$ in coeval deposits.

4.3. Evaluation of opal $\delta^{18}O$

In the following section, we will discuss potential influences of water and surface hydroxyls on the SIMS oxygen isotope analyses of opal. We will outline arguments based on our SIMS measurements that our

record of $\delta^{18}O$ reflects the primary opal oxygen isotope signature. Lastly, we will discuss the relationship between $\delta^{18}O$ and seepage water and the $\delta^{18}O$ of precipitation ($\delta^{18}O_{precip}$) and outline plausible interpretations of the PNP1 $\delta^{18}O$ record in the context of modern $\delta^{18}O_{precip}$.

4.3.1. Determining the influence of water on opal $\delta^{18}O$

Water is incorporated into covalently bonded silica in several ways. Molecular H_2O can occur as isolated molecules trapped within the silicate matrix, or as hydrogen-bonded H_2O on the surface of silica spherules, while chemically-bound OH is present as silanol groups on the surface of silica spherules or within the silica matrix (Langer and Flörke, 1974). Based on D/H isotope exchange experiments using diatomite, molecular water and a small fraction of the surface hydroxyls can exchange with ambient water at relatively low temperatures (25 to 100 °C). However, this exchangeable water fraction can be removed with extensive pumping under vacuum (Knauth and Epstein, 1982). Biogenic silica deposits, such as diatom frustules (Menicucci et al., 2013), which have large surface areas relative to our samples, may exchange 10 to 20% of their oxygen upon coming in contact with atmospheric water or water vapor (Labeyrie and Juillet, 1982). Typically, adsorbed H_2O and structural OH^- are removed prior to analysis by traditional mass spectrometric methods through heating under vacuum and/or stepwise or laser fluorination (e.g. Dodd and Sharp, 2010; Menicucci et al., 2013). For SIMS analysis, an unknown amount of the more labile water is removed when the samples are repeatedly dried in a vacuum oven at 210 mbar and 55 °C, stored in a desiccator

and then placed under moderate to high vacuum in the SEM and SIMS instruments ($\sim 7 \times 10^{-9}$ mbar for SHRIMP-RG analyses and $\sim 3 \times 10^{-8}$ mbar for CAMECA IMS 1280 analyses).

In order to monitor potential contribution of oxygen from the hydrous components of opal and to determine how this oxygen might influence the sample and standard $\delta^{18}O$, we measured the $^{16}OH/^{16}O$ of the UWQ-1, BZVV and PNP samples during SIMS analysis as a proxy for water in the analyzed sample volume. In detail, there are small differences in raw $^{16}OH/^{16}O$ ratios due to changes in the vacuum of the analysis chamber. As the standard UWQ-1, a granulite facies quartzite, is assumed to contain no water, we applied a background correction to each BZVV and unknown $^{16}OH/^{16}O$ measurement using the raw $^{16}OH/^{16}O$ of bracketing UWQ-1 measurements (Wang et al., 2014). The average raw $^{16}OH/^{16}O$ of UWQ-1 was 6.39×10^{-4} during the analytical period. The average background corrected $^{16}OH/^{16}O$ of the PNP1 opal is similar to that of the BZVV opal standard (2.49×10^{-3} vs. 1.60×10^{-3}, respectively). Although measurements of $^{16}OH/^{16}O$ are not calibrated for mg/kg [H], these data offer three lines of evidence suggesting that the measured values reflect the primary $\delta^{18}O$ signatures of the PNP opal:

(1) The instrumental mass fractionation observed for analyses of both quartz (UWQ-1) and opal (BZVV) standards is identical within error.
(2) The average measured $^{16}OH/^{16}O$ and $\delta^{18}O$ of BZVV on two separate mounts agree within analytical error (Fig. 8): mount 17 which was prepared in California where the composition of tap
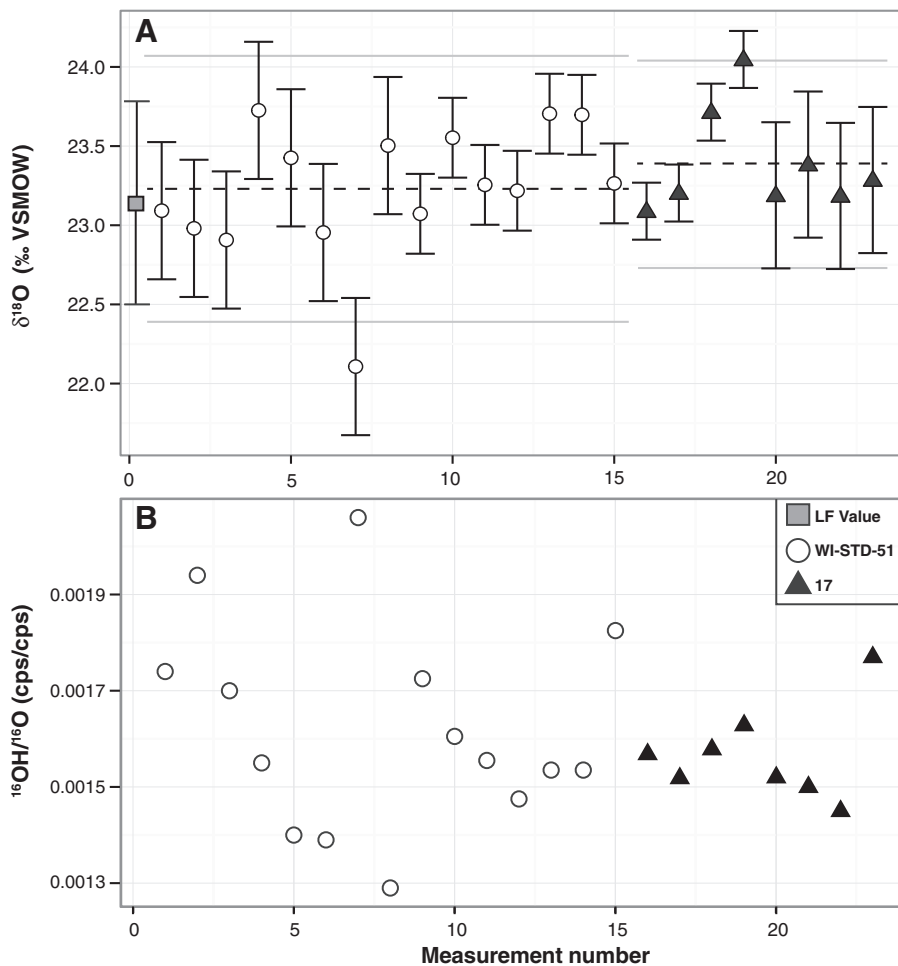
Fig. 8. A) Measured oxygen isotope values of opal standard BZVV from mount WI-STD-51 prepared at WiscSIMS (white circles), and mount 17 prepared at Stanford University in California (black triangles). Both mounts were analyzed at WiscSIMS. Values of $\delta^{18}O$ have been corrected for IMF using UWQ-1 and are given relative to VSMOW. Dashed lines are mean values for each group of standards and gray lines are 2SD. Gray square at x = 0 represents the bulk value of BZVV measured by laser fluorination (23.1 ± 0.6‰, 2SD, n = 4). B) Raw, background-corrected $^{16}OH/^{16}O$ ratios for the same analyses of BZVV.

water is −5.9 to −4.0‰, and WI-STD-51 prepared in Wisconsin where $\delta^{18}O$ of tap water is −7.9 to −6.0‰ (Bowen et al., 2007).

(3) We observe no correlation between the measured $\delta^{18}O$ of the PNP1 opal and $^{16}OH/^{16}O$ during the 20 cycles that comprise an individual measurement (Fig. 9) or over the course of the measurement period ($r = 0.22$, $p = 0.31$) (Fig. 10; Table 2). This suggests that the contribution of OH is similar for all spots and thus the amount of OH contributed by each sample is not

significantly influencing variations in $\delta^{18}O$. Samples from the two separate epoxy mounts (17 and 22) display overlapping values of both $\delta^{18}O$ and $^{16}OH/^{16}O$. Variations in sample $^{16}OH/^{16}O$ also display no spatial pattern in relation to position on the mount.

In summary, although we cannot definitively exclude artifacts introduced by O isotope exchange during sample preparation and storage,
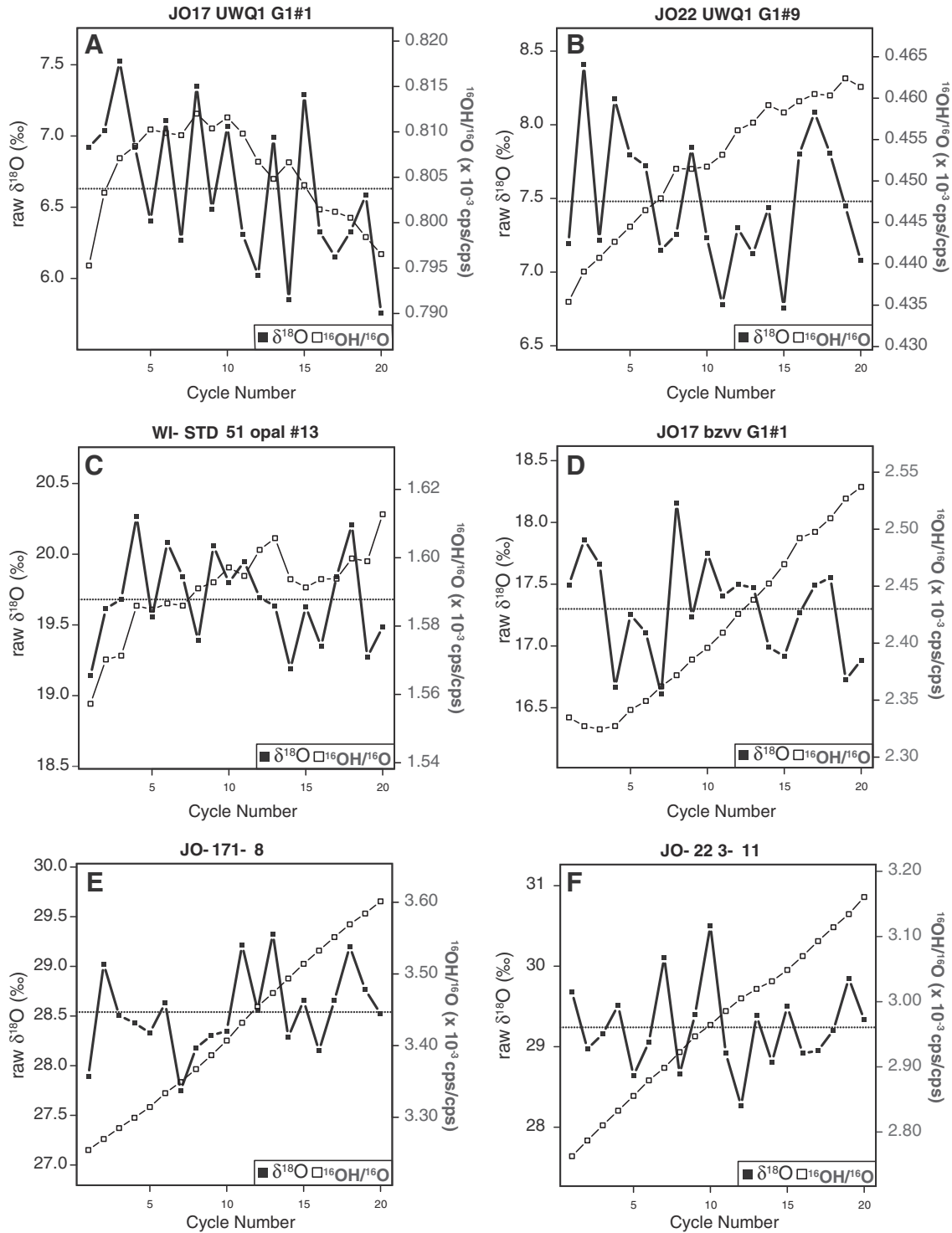
Fig. 9. Raw $\delta^{18}O$ (‰) and $^{16}OH/^{16}O$ (cps/cps) for the 20 cycles of a single-spot measurement for the homogeneous UWQ-1 quartz standard on mount 17 (A) and mount 22 (B), the BZVV opal standard for mount WI-STD 51 (C) mount 17 (D), and PNP1 opal from cross section 17-1a (E) and 22-3 (F). Dashed black horizontal lines show the final raw $\delta^{18}O$ for each spot measurement.
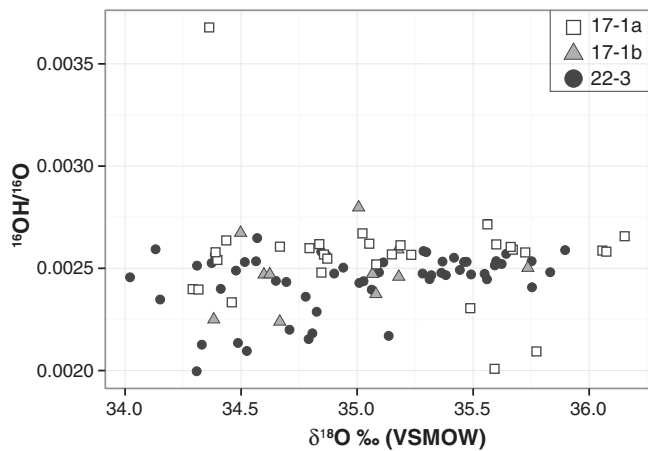
Fig. 10. PNP1 $\delta^{18}O$ (values corrected for IMF using UWQ-1 and given relative to VSMOW) versus background corrected raw $^{16}O^1H/^{16}O$ (cps/cps) for all $\delta^{18}O$ spot analyses shown in Fig. 4b and Table 2. For the entire dataset the Pearson product-moment correlation coefficient, $r = 0.22$, $p = 0.31$.

Table 4

Ion microprobe oxygen isotope values for calcite measured on PNP1 cross section 22-3 and bracketing UWC-3 calcite standard values.

Sample name	$\delta^{18}O$ ‰ VSMOW	Error 2SD	IMF ‰	$\delta^{18}O$ ‰ raw	Error 2SE
JO22c 3-66	27.52	0.43		22.97	0.18
JO22c 3-67	28.67	0.43		24.11	0.31
JO22c 3-68	24.88	0.43		20.35	0.27
JO22c 3-69	23.74	0.43		19.21	0.26
JO22c 3-70	26.48	0.43		21.94	0.27
JO22c 3-71	25.79	0.43		21.25	0.24
JO22c 3-73	28.68	0.43		24.12	0.26
JO22c 3-74	25.55	0.43		21.01	0.25
JO22c 3-75	25.94	0.43		21.39	0.25
Bracket UWC-3	12.49		−4.43	8.01	0.43
JO22c 3-76	26.59	0.26		21.79	0.20
JO22c 3-77	26.62	0.26		21.82	0.19
JO22c 3-79	27.26	0.26		22.46	0.22
JO22c 3-80	24.46	0.26		19.67	0.31
JO22c 3-81	24.87	0.26		20.08	0.18
JO22c 3-83	25.21	0.26		20.42	0.31
JO22c 3-84	25.53	0.26		20.74	0.16
JO22c 3-85	26.58	0.26		21.78	0.28
JO22c 3-86	26.23	0.26		21.43	0.26
Bracket UWC-3	12.49		−4.67	7.76	0.26

these lines of evidence suggest that the relative contribution of measured OH to the variability in PNP opal $\delta^{18}O$ is low. In particular, the lack of relationship between $\delta^{18}O$ and $^{16}OH/^{16}O$ suggest that measured $\delta^{18}O$ values of opal were not significantly influenced by $\delta^{18}O$ of water, that washing during the sample preparation process did not influence the $\delta^{18}O$ of opal, and that measured variations in $\delta^{18}O$ primarily reflect changes in the oxygen isotopic ratios of Si-O-Si.

4.3.2. Opal $\delta^{18}O$ as a record of seepage water $\delta^{18}O$

If the PNP1 opal was precipitated in isotopic equilibrium with seepage water, the measured opal $\delta^{18}O$ can be used to estimate seepage water $\delta^{18}O$, which will be related to $\delta^{18}O_{precip}$. Using the measured opal $\delta^{18}O$ and the average air temperature for PNP (15 °C), we calculate a range for the $\delta^{18}O$ of seepage water of −2.5 to −4.6‰ (VSMOW) (Kita et al., 1985). This overlaps with the range of modern $\delta^{18}O_{precip}$ at PNP (−2.3 to −14.7‰, average of −6.8‰) (Berkelhammer et al., 2012), suggesting that $\delta^{18}O$ precipitated in isotopic equilibrium with seepage water. The enrichment in ^{18}O of the calculated seepage water $\delta^{18}O$ relative to average modern precipitation might reflect evaporation of infiltrating waters that modifies the $\delta^{18}O$ signal and/or overall differences in $\delta^{18}O_{precip}$ during the mid-Holocene relative to today. It is also possible that temperature varied at PNP during the Holocene. Pollen records from the northern California Coast Range suggest the mid-Holocene was ~1 to 2 °C warmer than the early Holocene in some locations (Adam and West, 1983). If temperatures at PNP increased by 2 °C across the early to mid-Holocene, this could have led to an approximately 0.6‰ decrease in opal $\delta^{18}O$, assuming that water $\delta^{18}O$ remained constant. This is smaller than the change observed in the smoothed PNP1 record across the early-mid-Holocene (0.75‰) and represents the opposite trend from the increase in $\delta^{18}O$ that is observed during this time. This suggests that, while the potential influence of temperature change cannot be entirely ruled out, it is likely not the dominant influence on $\delta^{18}O$ at PNP.

We have also analyzed the $\delta^{18}O$ of intervening calcite layers of crosssection 22-3 by SIMS. Four consecutive measurements of the UWC-3 calcite standard ($\delta^{18}O = 12.49‰$ VSMOW; Kozdon et al., 2009) bracketed each set of 10–15 analyses of PNP1 calcite, i.e., four standard analyses occurred before and four after each unknown. The 2 SD precision on UWC-3 measurements was 0.49‰ ($n = 12$) over the measurement period, and the spot-to-spot analytical uncertainty for each block of samples was 0.35‰ on average. Measured $\delta^{18}O$ values for PNP1 calcite range from 23.7 to 28.7‰ (VSMOW) (Table 4). Using these measured values, the equilibrium fractionation of Kim and O'Neil (1997), and the average air temperature for PNP (15 °C), we calculate a range for the $\delta^{18}O$ of water that precipitated PNP1 calcite of −1.9 to −6.7‰. This range of values

encompasses that calculated for seepage water based on measured opal $\delta^{18}O$ values (−2.5 to −4.6‰) and also overlaps with the range of modern $\delta^{18}O_{precip}$ at PNP, lending further support to the interpretation that PNP $\delta^{18}O$ values, measured by SIMS, reflect seepage water $\delta^{18}O$.

It is possible that the depositional shifts between opal and calcite in PNP1 reflect seepage water variations related to climate. Interlaminated calcite and opal in speleothem deposits have been linked to variations in seepage water pH, with opal precipitation occurring at lower pH. This is thought to occur when silica saturation is increased after enhanced precipitation of carbonate along the seepage water flow path (Hill and Forti, 1997; Woo et al., 2008). Thus, periods of opal deposition within PNP1 may be biased toward intervals of enhanced calcite precipitation earlier in the seepage water flow path or potentially toward intervals of increased CO_2 concentrations in seepage waters that would act to lower pH. Enhanced calcite precipitation earlier in the flow path, known as "prior calcite precipitation" in cave environments, may result from slower flow rates due to a drier climate (e.g. Fairchild and Baker, 2012). Thus, it is possible that the opal layers in PNP1 oversample past dry intervals.

Seepage water $\delta^{18}O$ values calculated from both PNP1 opal and calcite overlap with the high $\delta^{18}O$ end of the range of modern $\delta^{18}O_{precip}$. The variability in opal $\delta^{18}O$ likely reflects changes in $\delta^{18}O_{precip}$ through time with some potential influence by evaporation of soil waters. Opal $(^{234}U/^{238}U)_0$ is uniquely sensitive to P-ET, and so the increases in $(^{234}U/^{238}U)_0$ and $\delta^{18}O$ during the early Holocene may each reflect decreasing P-ET, with the $\delta^{18}O$ responding to increasing evaporation of seepage waters. However, the $(^{234}U/^{238}U)_0$ record does not point to a significant increase in P-ET during the mid-late Holocene, while the opal $\delta^{18}O$ record displays a decrease of similar magnitude to the early Holocene increase. It is possible that evaporation and precipitation each decreased at this time, such that P-ET remained steady. However, it is also possible is that $\delta^{18}O_{precip}$ varied across the Holocene and this variability is captured in opal $\delta^{18}O$. Modern rainfall $\delta^{18}O_{precip}$ at PNP shows no significant correlation with precipitation amount, displays only a weak negative correlation with relative humidity ($r^2 = 0.2$, $p \leq 0.001$), and is primarily linked to moisture source, with higher $\delta^{18}O_{precip}$ associated with subtropical Pacific storms and lower $\delta^{18}O_{precip}$ with North Pacific storms (Fig. 1) (Berkelhammer et al., 2012). Given this relationship between modern $\delta^{18}O_{precip}$ and moisture source at Pinnacles as well as other locations in southern and central California (Oster et al., 2012b; McCabe-Glynn et al., 2013), it is likely that shifts in $\delta^{18}O$ at least in part reflect changes in the primary moisture source for precipitation reaching the central California Coast Range.

4.3.3. Utility of opal $\delta^{18}O$ and future work

Enhanced spatial coverage of paleoclimate reconstructions is increasingly important for evaluating climate models used to link proxy data from point measurements to climate mechanisms (Oster et al., 2015, Harrison et al., 2015). Although high-resolution paleoclimate records from well-dated archives, such as speleothems, provide key windows into both high-frequency and long-term climate shifts, lower resolution records that can fill gaps in space and time remain critical. Our first attempt to develop fine-scale records of $\delta^{18}O$ in opal suggests that coupled SIMS $\delta^{18}O$ and $(^{234}U/^{238}U)_0$ measurements of high-U opal may provide a new approach for developing terrestrial paleoclimate records in regions or during intervals where ice, lake sediment and speleothem records are unavailable or where pedogenic carbonate is present but not reliably datable due to, for example, low U concentrations.

Our analysis indicates that authigenic opal deposits are capable of providing records of paleoclimatic change of comparable temporal resolution to pedogenic carbonate records (e.g. Amundson et al., 1996; Oerter et al., 2016). Furthermore, the extension of these methods to opal would allow for an additional, datable material commonly found in semi-arid environments where pedogenic carbonate may be absent. However, although our analysis demonstrated that the PNP1 opal $\delta^{18}O$ is reproducible at small spatial scales, the degree of scatter in the time series suggests some variability in $\delta^{18}O$ on the 100's of microns to cm scale. As mentioned previously, this degree of scatter present in the PNP $\delta^{18}O$ record is comparable to that noted in a similar SIMS analysis of pedogenic carbonates (Oerter et al., 2016) and may be characteristic of these deposits, where there is inherent difficulty in determining coeval material over mm to cm distances. This scatter may reflect slightly different degrees of evaporation and seepage water modification along flow paths within the soil zone and along the host rocks prior to deposition. For longer lived deposits from the continental interior, such as the Wind River pedogenic carbonates (Oerter et al., 2016), this scatter is a much smaller proportion of the overall variability in $\delta^{18}O$ documented by the deposit. Here, paleoclimate records suggest variations of several permil in $\delta^{18}O_{precip}$ during the last glacial period, which is covered by the Wind River deposit (e.g. Lachniet et al., 2014). However, much smaller variations $\delta^{18}O_{precip}$ typically occur in coastal environments, as changes in $\delta^{18}O_{precip}$ driven by source and trajectory over the ocean are not further amplified by distillation as air masses travel inland (Vachon et al., 2010). This is reflected in other coastal paleoclimate records of $\delta^{18}O$ variability, such as speleothems (Vacco et al., 2005; Oster et al., 2009; Ersek et al., 2012). By comparison the Oregon Caves speleothem record from the Klamath Mountains north of PNP records variation of ~1.75‰ over approximately the same interval covered by the PNP1 opal (5–13 ka) (Ersek et al., 2012).

Given the inherent variability at this scale, samples with more uniform growth history will be critical for future work as uncertainty in the age model accentuates the natural variability. A longer-lived record of opal $\delta^{18}O$ variability from a more continental location might also help to distinguish whether the scatter evident in the PNP record is related to these factors. Likewise, the analysis of multiple samples from the same location covering a larger spatial extent (meter scale) would provide a necessary check for reproducibility of potential climate signals – something which was only tested at a small scale in this study due to sampling restrictions in the national park. Lastly, further investigation of the conditions for and kinetics of oxygen and silicon isotope exchange between amorphous silica and water through laboratory investigations (e.g., Pollington et al., 2016) and the effects of incorporation of water in SIMS analyses would improve the utility of this new proxy.

4.4. Implications of PNP $(^{234}U/^{238}U)_0$ and $\delta^{18}O$ records for western US climate during the Holocene

Assuming the PNP deposit faithfully records the climate signals described above, the records of $(^{234}U/^{238}U)_0$ and $\delta^{18}O$ variability for the finely laminated PNP opal provide information about hydrologic and moisture source changes for coastal California on millennial time scales

during Holocene. The $(^{234}U/^{238}U)_0$ record indicates a decrease in P-ET of 12 to 30% between 14.0 ± 2.3 ka and 6.5 ± 0.5 ka and little change in P-ET following 6.5 ka. The rise in opal $\delta^{18}O$ until ~6.5 ka suggests an increasing component of subtropical Pacific water vapor and/or increasing evaporation, while the decline in $\delta^{18}O$ after ~6.5 ka suggests a shift to more North Pacific water vapor. Although slow growth rates and age uncertainties on the PNP1 proxies preclude comparison of anything finer than multi-millennial-scale trends, these inferences are broadly consistent with climatic shifts inferred for this region from other Holocene paleoclimate records, as described below.

The lack of variability in the smoothed $(^{234}U/^{238}U)_0$ after ~6.5 ka requires that the shift in dominant water vapor source was not accompanied by a significant change in P-ET. The $(^{234}U/^{238}U)_0$ record indicates that P-ET reached a minimum at ~6.5 ka and remained relatively low for the duration of the PNP record (until ~2.7 ka). This observation is consistent with a number of paleoclimate records from Sierra Nevada lakes, including Swamp Lake (SL, Fig. 1a) and Pyramid Lake (PL, Fig. 1a) that suggest dry and warm conditions during the early middle Holocene (7.6 to 6.3 ka) (Benson et al., 2002; Mensing et al., 2004; Street et al., 2012). Tree stumps rooted below modern lake levels in and near Lake Tahoe (LT, Fig. 1a) indicate precipitation during the middle Holocene dropped by at least 40% compared to modern values (Kleppe et al., 2011). Marine pollen records from northern and southern California also indicate arid conditions at ~7 ka (Fig. 11) (Heusser, 1998; Barron et al., 2003).

In contrast, a prominent pluvial event between 6.3 and 6.9 ka, possibly linked to the increased occurrence of subtropically-derived atmospheric river storms (Fig. 1a), is indicated by two lake records from
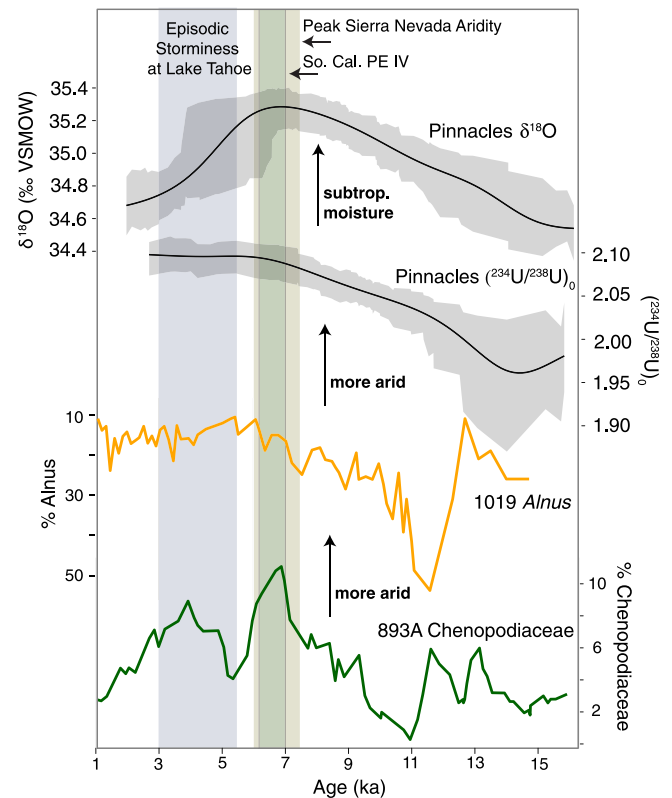

Fig. 11. Profiles vs. age, from top to bottom: opal PNP1 $\delta^{18}O$ and $(^{234}U/^{238}U)_0$ (this study); percent *Alnus* pollen from ODP site 1019 (Barron et al., 2003); and percent Chenopodiaceae pollen from ODP site 893A (Heusser, 1998). Brown bar highlights peak arid conditions noted in Sierra Nevada lake records (Benson et al., 2002; Mensing et al., 2004; Street et al., 2012). Green bar highlights Pluvial Event IV noted in southern California lake records (Kirby et al., 2012). Blue bar highlights increased storminess noted from Lake Tahoe turbidite deposits (Osleger et al., 2009) (See Fig. 1 for location of proxy records).

southern California (Kirby et al., 2012) (LBL and LE, Fig. 1a). Although the low temporal resolution of the PNP1 record precludes our ability to resolve this sub-millennial event, the increase in opal $\delta^{18}O$ through the early Holocene is consistent with increased advection of subtropical moisture to California at this time. However, the reduction in P-ET at PNP through the early to mid-Holocene indicates that the enhanced moisture availability that lead to these pluvial events may have been confined to Southern California.

The decrease in opal $\delta^{18}O$ following ~6 ka, accompanied by invariant $(^{234}U/^{238}U)_0$, suggests a shift to more North Pacific sourced moisture that did not lead to a measurable change in P-ET at PNP. Between ~5 and 3 ka, Sierra Nevada lake records indicate reduced aridity punctuated by intermittent wet and dry phases (Mensing et al., 2004) and increased storminess (Osleger et al., 2009). Lake sediments from southern Oregon (BL, Fig. 1a) suggest cooler and wetter conditions to the north (Briles et al., 2005), while pollen from the Santa Barbara Basin indicates only a slight decrease in aridity further south (Fig. 11) (Heusser, 1998). Thus, it is possible that a late Holocene increase in winter storms from the North Pacific eased drought in Northern California but caused only small or sporadic decreases in aridity along the coast and in the mountains of central California.

The $(^{234}U/^{238}U)_0$ and $\delta^{18}O$ from PNP1 are consistent with increasing aridity in the central California Coast Ranges during the early middle-Holocene, but suggest conditions here may not have been as severe as the inland mega-droughts noted in Sierran lakes. The moderate (12–30%) decrease in P-ET across the early Holocene as suggested by the PNP $(^{234}U/^{238}U)_0$ record therefore indicates that the hydroclimatic changes in the central California Coast Range might have been smaller than the >40% decrease in precipitation relative to modern inferred for the Tahoe Basin (Kleppe et al., 2011). However, more quantitative estimates of precipitation decrease are necessary to determine the severity of drought across this region.

The shift to more subtropical moisture leading up to ~6 ka, and more North Pacific moisture afterward is consistent with regional terrestrial and marine proxy records that suggest the North Pacific high pressure cell was situated further to the north during the early Holocene, weakening the California Current, and allowing moisture from the subtropical and tropical Pacific to penetrate into California. During the late Holocene, the PNP1 records are consistent with the hypothesis that the North Pacific High shifted southward, the Aleutian Low intensified, and more North Pacific sourced moisture was channeled into California (Barron and Andersen, 2011).

5. Conclusions

We have presented an evaluation of authigenic opal deposits as paleoclimate archives through in situ analysis of $(^{234}U/^{238}U)_0$ and $\delta^{18}O$ in an opal deposit from Pinnacles National Park in central California. Coupled $(^{234}U/^{238}U)_0$ and $\delta^{18}O$ from Pinnacles National Park provide information about net infiltration and moisture source variability in the central California Coast Range during the Holocene. Opal $(^{234}U/^{238}U)_0$ document a moderate (12–30%) decrease in net infiltration from around 14 to 6 ka, coincident with the timing of increasing aridity inferred from Sierra Nevada lake records. Oxygen isotope variations in the PNP opal deposit likely reflect moisture source though some influence of seepage water evaporation cannot be ruled out. The PNP $\delta^{18}O$ record indicates that precipitation in the central California Coast Ranges was increasingly influenced by subtropical storms rather than North Pacific-sourced storms at the same period when the $(^{234}U/^{238}U)_0$ suggests increased aridity. A shift to more North Pacific sourced storms commenced after ~5 ka coincident with the easing of aridity in Northern California and increased storminess in the Sierra Nevada as indicated by lake sediment records. Taken together the PNP $(^{234}U/^{238}U)_0$ and $\delta^{18}O$ records indicate that the timing of precipitation changes was similar between coastal and inland locations in central California, but the magnitude of these variations was larger inland, and that the mid-

Holocene mega-droughts inferred from inland lakes in the Sierra Nevada were significantly milder on the coast.

Our results suggest that useful insights about past hydrologic change can be gleaned from authigenic opal deposits, and that these deposits have the potential to enhance the spatial and temporal coverage of paleoclimate reconstructions in regions where other archives (e.g., lakes, speleothems) might be scarce. However, further studies of isotopic variability in opal are needed to improve the utility of this archive. In particular, further study of the influence of water in opal on $\delta^{18}O$ variability and additional in situ analysis of $\delta^{18}O$ variability on longer-lived opal deposits with uniform growth histories from more continental locations are necessary to verify the controls on this potential proxy. Similarly, further investigation into short-term and spatial variability in $(^{234}U/^{238}U)_{sw}$ will improve qualitative and quantitative applications of the $(^{234}U/^{238}U)_0$ in both authigenic opal and carbonate deposits.

Supplementary data to this article can be found online at http://dx.doi.org/10.1016/j.chemgeo.2016.12.009.

References

Adam, D.P., West, G.J., 1983. Temperature and precipitation estimates through the last glacial cycle from Clear Lake, California, Pollen Data. Science 219, 168–170.

Aggarwal, P.K., Romatschke, U., Araguas-Araguas, L., Belachew, D., Longstaffe, F., Berg, P., Schumacher, C., Funk, A., 2016. Proportions of convective and stratiform precipitation revealed in water isotope ratios. Nat. Geosci. http://dx.doi.org/10.1038/ngeo2739.

Alexandre, A., Meunier, J.-D., Llorens, E., Hill, S.M., Savin, S.M., 2004. Methodological improvements for investigating silcrete formation: petrography, FT-IR and oxygen isotope ratio of silcrete quartz cement, Lake Eyre Basin (Australia). Chem. Geol. 211, 261–274.

Amelin, Y., Back, M., 2006. Opal as a U-Pb geochronometer: search for a standard. Chem. Geol. 232, 67–86.

Amundson, R., Chadwick, O.A., Kendall, C., Wang, Y., DeNiro, M., 1996. Isotopic evidence for shifts in atmospheric circulation patterns during the late Quaternary in mid-North America. Geology 24, 23–26.

Andersen, M.B., Erel, Y., Boudon, B., 2009. Experimental evidence for ^{234}U-^{238}U fractionation during weathering with implications for $^{234}U/^{238}U$ in natural waters. Geochim. Cosmochim. Acta 73 (14), 4124–4141.

Ayalon, A., Bar-Matthews, M., Kaufman, A., 1999. Petrography, strontium, barium, and uranium concentrations, and strontium and uranium isotopic ratios in speleothems as paleoclimatic proxies: Soreq Cave, Israel. The Holocene 9. http://dx.doi.org/10.1191/095968399673664163.

Barron, J.A., Andersen, L., 2011. Enhanced Late Holocene ENSO/PDO expression along the margins of the eastern North Pacific. Quat. Int. 235, 3–12.

Barron, J.A., Heusser, L., Herbert, T., Lyle, M., 2003. High-resolution climatic evolution of coastal northern California during the past 16,000 years. Paleoceanography 18. http://dx.doi.org/10.1029/2002PA000768.

Benson, L., Kashgarian, M., Rye, R., Lund, S., Paillet, F., Smoot, J., Kester, C., Mensing, S., Meko, D., Lindström, S., 2002. Holocene multidecadal and multicentennial droughts affecting Northern California and Nevada. Quat. Sci. Rev. 21, 659–682.

Berkelhammer, M., Stott, L., Yoshimura, K., Johnson, K., Sinha, A., 2012. Synoptic and mesoscale controls on the isotopic composition of precipitation in the western United States. Clim. Dyn. 38, 433–454.

Blisniuk, P.M., Sharp, W.D., 2003. Rates of late Quaternary normal faulting in central Tibet from U-series dating of pedogenic carbonate in displaced fluvial gravel deposits. Earth Planet. Sci. Lett. 215, 169–186.

Blisniuk, K., Oskin, M., Fletcher, K., Rockwell, T., Sharp, W.D., 2012. Assessing the reliability of U-series and 10Be dating techniques on alluvial fans in the Anza Borrego Desert, California. Quat. Geochronol. 13, 26–41.

Bourdon, B., Bureau, S., Andersen, M., Pili, E., Hubert, A., 2009. Weathering rates from top to bottom in a carbonate environment. Chem. Geol. 258, 275–287.

Bowen, G.J., Ehleringer, J.R., Chesson, L.A., Stange, E., Cerling, T.E., 2007. Stable isotope ratios of tap water in the contiguous United States. Water Resour. Res. 43. http://dx.doi.org/10.1029/2006WR005186.

Briles, C.E., Whitlock, C., Bartlein, P.J., 2005. Postglacial vegetation, fire, and climate history of the Siskiyou Mountains, Oregon, USA. Quat. Res. 64, 44–56.

Cerling, T.E., 1984. The stable isotopic composition of modern soil carbonate and its relationship to climate. Earth Planet. Sci. Lett. 71, 229–240.

Chabaux, F., Riotte, J., Clauer, N., France-Lanord, C., 2001. Isotopic tracing of the dissolved U fluxes of Himalayan rivers: implications for present and past U budgets of the Ganges-Brahmaputra system. Geochim. Cosmochim. Acta 65, 3201–3217.

Chamberlain, C.P., Poage, M.A., 2000. Reconstructing the paleotopography of mountain belts from the isotopic composition of authigenic minerals. Geology 28, 115–118.

Chamberlain, C.P., Mix, H.T., Mulch, A., Hren, M.T., Kent-Corson, M.L., Davis, S.J., Horton, T.W., Graham, S.A., 2012. The Cenozoic climatic and topographic evolution of the western North American Cordillera. Am. J. Sci. 312, 213–262.

Chaudhuri, P., Marron, J.S., 1999. SiZer for exploration of structures in curves. J. Am. Stat. Assoc. 94, 807–823.

Cheng, H., Edwards, R.L., Hoff, J., Gallup, C.D., Richards, D.A., Asmerom, Y., 2000. The half-lives of uranium-234 and thorium-230. Chem. Geol. 169, 17–33.

Dansgaard, W., 1964. Stable isotopes in precipitation. Tellus 16, 436–468.

Dettinger, M., 2011. Climate change, atmospheric rivers, and floods in California – a multimodel analysis of storm frequency and magnitude changes. J. Am. Water Resour. Assoc. 47, 514–523.

Dodd, J.P., Sharp, Z.D., 2010. A laser fluorination method for oxygen isotope analysis of biogenic silica and a new oxygen isotope calibration of modern diatoms in freshwater environments. Geochim. Cosmochim. Acta 74, 1381–1390.

Durand, S., Chabaux, F., Rihs, S., Duringer, P., Elsass, P., 2005. U isotope ratios as tracers of groundwater inputs into surface waters: example of the Upper Rhine hydrosystem. Chem. Geol. 220, 1–19.

Edwards, R.L., Cheng, H., Murrell, M.T., Goldstein, S.J., 1997. Protactinium-231 dating of carbonates by thermal ionization mass spectrometry: implications for Quaternary climate change. Science 276, 782–786.

Ersek, V., Clark, P.U., Mix, A.C., Cheng, H., Edwards, R.L., 2012. Holocene winter climate variability in mid-latitude western North America. Nat. Commun. 3, 1219.

Fairchild, I.J., Baker, A., 2012. Speleothem Science: From Process to Past Environments. Wiley-Blackwell (450 pp.).

Frumkin, A., Stein, M., 2004. The Sahara-East Mediterranean dust and climate connection revealed by strontium and uranium isotopes in a Jerusalem speleothem. Earth Planet. Sci. Lett. 217, 451–464.

Graham, C.M., Valley, J.W., Winter, B.L., 1996. Ion microprobe analysis of 18O/16O in authigenic and detrital quartz in the St. Peter Sandstone, Michigan Basin and Wisconsin Arch, USA: contrasting diagenetic histories. Geochim. Cosmochim. Acta 60, 5101–5116.

Guerrero, J.L., Vallejos, A., Cerón, Sánchez-Martos, F., Pulido-Bosch, A., Bolivar, J.P., 2016. U-isotopes and 226Ra as tracers of hydrogeochemical processes in carbonated karst aquifers from arid areas. J. Environ. Radioact. 158-159, 9–20.

Harrison, S.P., Bartlein, P.J., Izumi, K., Li, G., Annan, J., Hargreaves, J., Braconnot, P., Kageyama, M., 2015. Evaluation of CMIP5 palaeo-simulations to improve climate predictions. Nat. Clim. Chang. 5, 735–743.

Hellstrom, J.C., McCulloch, M.T., 2000. Multi-proxy constraints on the climatic significance of trace element records from a New Zealand speleothem. Earth Planet. Sci. Lett. 179, 287–297.

Heusser, L., 1998. Direct correlation of millennial-scale changes in western North American vegetation and climate changes in the California current system over the past ~60 kyr. Paleoceanography 13, 252–262.

Hill, C.A., Forti, P., 1997. Cave Minerals of the World. National Speleological Society, Huntsville, AL (463 pp.).

Hubert, A., Bourdon, B., Pili, E., Meynadier, L., 2006. Transport of radionuclides in an unconfined chalk aquifer inferred from U-series disequilibria. Geochim. Cosmochim. Acta 70, 5437–5454.

Ibarra, D.E., Egger, A.E., Weaver, K.L., Harris, C.R., Maher, K., 2014. Rise and fall of late Pleistocene pluvial lakes in response to reduced evaporation and precipitation: evidence from Lake Surprise, California. Geol. Soc. Am. Bull. http://dx.doi.org/10.1130/B31014.1.

Kaufman, A., Broecker, W., 1965. Comparison of 230Th and 14C ages for carbonate materials from lakes Lahontan and Bonneville. J. Geophys. Res. 70, 4039.

Kaufman, A., Wasserburg, G.J., Porcelli, D., Bar-Matthews, M., Ayalon, A., Halicz, L., 1998. U-Th isotope systematics from the Soreq cave, Israel and climatic correlations. Earth Planet. Sci. Lett. 156, 141–155.

Kelly, J.L., Fu, B., Kita, N.T., Valley, J.W., 2007. Optically continuous silcrete quartz cements of the St. Peter Sandstone: high precision oxygen isotope analysis by ion microprobe. Geochim. Cosmochim. Acta 71, 3812–3832.

Kigoshi, K., 1971. Alpha-recoil thorium-234 – dissolution into water and uranium-234/uranium-238 disequilibrium in nature. Science 173, 47–49.

Kim, S.-T., O'Neil, J.R., 1997. Equilibrium and nonequilibrium oxygen isotope effects in synthetic carbonates. Science 61, 3461–3475.

Kirby, M.E., Zimmerman, S.R.H., Paterson, W.P., Rivera, J.J., 2012. A 9170-year record of decadal to multi-centennial scale pluvial episodes from the coastal Southwest United States: a role for atmospheric rivers? Quat. Sci. Rev. 46, 57–65.

Kita, I., Taguchi, S., Matsubaya, O., 1985. Oxygen isotope fractionation between amorphous silica and water at 34–93 °C. Nature 314, 83–84.

Kita, N.T., Ushikubo, T., Fu, B., Valley, J.W., 2009. High precision SIMS oxygen isotope analysis and the effect of sample topography. Chem. Geol. 264, 43–57.

Kleppe, J.A., Brothers, D.S., Kent, G.M., Biondi, F., Jensen, S., Driscoll, N.W., 2011. Duration and severity of Medieval drought in the Lake Tahoe Basin. Quat. Sci. Rev. 30, 3269–3279.

Knauth, L.P., Epstein, S., 1982. The nature of water in hydrous silica. Am. Mineral. 67, 510–520.

Kozdon, R., Ushikubo, T., Kita, N.T., Spicuzza, M., Valley, J.W., 2009. Intratest oxygen isotope variability in planktonic foraminifera: new insights from in situ measurements by ion microprobe. Chem. Geol. 258, 327–337.

Kraemer, T.F., Brabets, T.P., 2012. Uranium isotopes ($^{234}U/^{238}U$) in rivers of the Yukon Basin (Alaska and Canada) as an aid in identifying water sources, with implications for monitoring hydrologic changes in arctic regions. Hydrogeol. J. 20, 469–481.

Labeyrie, L.D., Juillet, A., 1982. Oxygen isotopic exchangeability of diatom valve silica – interpretation and consequences for paleoclimatic studies. Geochim. Cosmochim. Acta 46, 967.

Lachniet, M.S., Denniston, R.F., Asmerom, Y., Polyak, V.J., 2014. Orbital control of western North America atmospheric circulation and climate over two glacial cycles. Nat. Commun. 5, 3805.

Langer, K., Flörke, O.W., 1974. Near infrared adsorption spectra (4000–9000 cm⁻¹) of opals and the role of "water" in these SiO₂-nH₂O minerals. Fortschr. Mineral. 52, 17–51.

Lindström, S., 1990. Submerged tree stumps as indicators of mid-Holocene aridity in the Lake Tahoe Basin. J. Calif. Gt. Basin Anthropol. 12, 146–157.

Ludwig, K.R., 2003. User's Manual for Isoplot 3.00: A Geochronological Toolkit for Microsoft Excel (Berkeley, CA).

Ludwig, K.R., Paces, J.B., 2002. Uranium-series dating of pedogenic silica and carbonate, Crater Flat, Nevada. Geochim. Cosmochim. Acta 66, 487–506.

Maher, K., 2010. The dependence of chemical weathering rates on fluid residence time. Earth Planet. Sci. Lett. 294, 101–110.

Maher, K., DePaolo, D.J., Christensen, J.N., 2006. U-Sr isotopic speedometer: fluid flow and chemical weathering rates in aquifers. Geochim. Cosmochim. Acta 70, 4417–4435.

Maher, K., Paces, J.B., Wooden, J., Miller, D.M., 2007. 230Th/U dating of surficial deposits using the ion microprobe (SHRIMP-RG): a microstratigraphic perspective. Quat. Int. 66, 15–28.

Maher, K., Ibarra, D.E., Oster, J.L., Miller, D.M., Redwine, J.L., Reheis, M.C., Harden, J.W., 2014. Uranium isotopes in soils as a proxy for past infiltration and precipitation across the western United States. Am. J. Sci. 314, 821–857.

McCabe-Glynn, S., Johnson, K.R., Strong, C., Berkelhammer, M., Sinha, A., Cheng, H., Edwards, R.L., 2013. Variable North Pacific influence on drought in southwestern North America since CEAD 854. Nat. Geosci. 6, 617–621.

McGee, D., Quade, J., Edward, R.L., Broecker, W.S., Cheng, H., Reiners, P.W., Evenson, N., 2012. Lacustrine cave carbonates: Novel archives of paleohydrologic change in the Bonneville Basin (Utah, USA). Earth Planet. Sci. Lett. 351-352, 182–194.

Menicucci, A.J., Matthews, J.A., Spero, H.J., 2013. Oxygen isotope analysis of biogenic opal and quartz using a novel microfluorination technique. Rapid Commun. Mass Spectrom. 27, 1–9.

Mensing, S.A., Benson, L.V., Kashgarian, M., Lund, S., 2004. A Holocene pollen record of persistent droughts from Pyramid Lake, Nevada, USA. Quat. Res. 62, 29–38.

Neymark, L.A., 2011. Potential effects of alpha-recoil on uranium-series dating of calcrete. Chem. Geol. 282, 98–112.

Neymark, L.A., Paces, J.B., 2013. Ion-probe U-Pb dating of authigenic and detrital opal from Neogene-Quaternary alluvium. Earth Planet. Sci. Lett. 361, 98–109.

Neymark, L.A., Amelin, Y., Paces, J.B., Petermen, Z.E., 2002. U-Pb ages of secondary silica at Yucca Mountain, Nevada: implications for the paleohydrology of the unsaturated zone. Appl. Geochem. 17, 709–734.

Nuriel, P., Weinberger, R., Rosenbaum, G., Golding, S.D., Zhao, J., Uysal, I.T., Bar-Matthews, M., Gross, M.R., 2012. Timing and mechanism of late-Pleistocene calcite vein formation across the Dead Sea Fault Zone, northern Israel. J. Struct. Geol. 36, 43–54.

Oerter, E.J., Sharp, W.D., Oster, J.L., Ebeling, A., Valley, J.W., Kozdon, R., Orland, I.J., Hellstrom, J., Woodhead, J.D., Hergt, J.M., Chadwick, O.A., Amundson, R., 2016. Pedothem carbonates reveal anomalous North American atmospheric circulation 70,000 to 55,000 years ago. Proc. Natl. Acad. Sci., 201515478

Osleger, D.A., Heyvaert, A.C., Stoner, J.S., Verosub, K.L., 2009. Lacustrine turbidites as indicators of Holocene storminess and climate: Lake Tahoe, California and Nevada. J. Paleolimnol. 42, 103–122.

Oster, J.L., Montañez, I.P., Sharp, W.D., Cooper, K.M., 2009. Late Pleistocene California droughts during deglaciation and Arctic warming. Earth Planet. Sci. Lett. 288, 434–443.

Oster, J.L., Ibarra, D.I., Harris, C.R., Maher, K., 2012a. Influence of eolian deposition and rainfall amounts on the U-isotopic composition of soil water and soil minerals. Geochim. Cosmochim. Acta 88, 146–166.

Oster, J.L., Montañez, I.P., Kelley, N.P., 2012b. Response of a modern cave system to large seasonal precipitation variability. Geochim. Cosmochim. Acta 91, 92–108.

Oster, J.L., Ibarra, D.E., Winnick, M.J., Maher, K., 2015. Steering of westerly storms over western North America at the Last Glacial Maximum. Nat. Geosci. 8, 201–205.

Paces, J.B., Ludwig, K.R., Peterman, Z.E., Neymark, L.A., 2002. $^{234}U/^{238}U$ evidene for local recharge patterns of groundwater flow in the vicinity of Yucca Mountain, Nevada, USA. Appl. Geochem. 17, 751–779.

Paces, J.B., Wurster, F.C., 2014. Natural uranium and strontium isotope tracers of water sources and surface water-groundwater interactions in arid wetlands – Pahranagat Valley, Nevada, USA. J. Hydrol. 517, 213–225.

Paces, J.B., Neymark, L.A., Wooden, J.L., Persing, H.M., 2004. Improved spatial resolution for U-series dating of opal at Yucca Mountain, Nevada, USA, using ion-microprobe and microdigestion methods. Geochim. Cosmochim. Acta 68, 1591–1606.

Paces, J.B., Neymark, L.A., Whelan, J.F., Wooden, J.L., Lund, S.P., Marshall, B.D., 2010. Limited hydrologic response to Pleistocene climate change in deep vadose zones – Yucca Mountain, Nevada. Earth Planet. Sci. Lett. 300, 287–298.

Page, F.Z., Ushikubo, T., Kita, N.T., Riciputi, L.R., Valley, J.W., 2007. High-precision oxygen isotope analysis of pictogram samples reveals 2 μm gradients and slow diffusion in zircon. Am. Mineral. 92, 1772–1775.

Pollington, A.D., Kozdon, R., Anovitz, L.M., Georg, R.B., Spicuzza, M.J., Valley, J.W., 2016. Experimental calibration of silicon and oxygen isotope fractionation between quartz and water at 250 °C by in situ microanalysis of experimental products and application to natural samples. Chem. Geol. 421, 127–142.

Polyak, V.J., Asmerom, Y., Burns, S.J., Lachniet, M.S., 2012. Climatic backdrop to the terminal Pleistocene extinction of North American mammals. Geology http://dx.doi.org/10.1130/G33226.1.

Porcelli, D., Swarzenski, P.W., 2003. The Behavior of U- and Th-Series Nuclides in Groundwater. Uranium-series Geochemistry Vol. 52 pp. 317–361.

R Core Team, 2012. R: A Language and Environment for Statistical Computing. R Foundation for Statistical Computing, Vienna, Austria 3-900051-07-0 (http://www.R-project.org/).

Rehfeld, K., Marwan, N., Heitzig, J., Kurths, J., 2011. Comparison of correlation analysis techniques for irregularly sampled time series. Nonlinear Process. Geophys. 18, 389–404.

Riotte, J., Chabaux, F., 1999. (^{234}U/^{238}U) activity ratios in freshwaters as tracers of hydrological processes: the Stengbach watershed (Vosges, France). Geochim. Cosmochim. Acta 63, 1263–1275.

Robinson, L.F., Henderson, G.M., Hall, L., Matthews, I., 2004. Climatic control of riverine and seawater uranium-isotope ratios. Science 305, 851–854.

Robinson, A.C., Owen, L.A., Chen, J., Schoenbohm, L.M., Hedrick, K.A., Blisniuk, K., Sharp, W.D., Imbrecke, D.B., Li, W., Yuan, Z., Caffee, M.W., Mertz-Kraus, R., 2015. No late Quaternary strik-slip motion along the northern Karakoram fault. Earth Planet. Sci. Lett. 409, 290–298.

Schaffhauser, T., Chabaux, F., Ambroise, B., Lucas, Y., Stille, P., Reuschlé, T., Perrone, T., Fritz, B., 2014. Geochemical and isotopic (U, Sr) tracing of water pathways in the granitic Ringelbach catchment (Vosges Mountains, France). Chem. Geol. 374-375, 117–127.

Scholz, D., Hoffman, D.L., 2011. StalAge – An algorithm designed for construction of speleothem age models. Quat. Geochronol. 6, 369–382.

Sharp, W.D., Ludwig, K.R., Chadwick, O.A., Amundson, R., Glaser, L.L., 2003. Dating fluvial terraces by ^{230}Th/U on pedogenic carbonate, Wind River Basin, Wyoming. Quat. Res. 59, 139–150.

Sheather, S.J., Jones, M.C., 1991. A reliable data-based bandwidth selection method for kernel density estimation. J. R. Stat. Soc. B 53, 683–690.

Sonderegger, D., 2011. SiZer: significant zero crossings. R Package Version 0.1–4 (http://CRAN.R-project.org/package=SiZer).

Spicuzza, M.J., Valley, J.W., McConnell, V.S., 1998. Oxygen isotope analysis of whole rock via laser fluorination: an air-lock approach. GSA Abstr. Programs.

Stern, L.A., Chamberlain, C.P., Reynolds, R.C., Johnson, G.D., 1997. Oxygen isotope evidence of climate change from pedogenic clay minerals in the Himalayan molasse. Geochim. Cosmochim. Acta 61, 731–744.

Street, J.H., Anderson, R.S., Paytan, A., 2012. An organic geochemical record of Sierra Nevada climate since the LGM from Swamp Lake, Yosemite. Quat. Sci. Rev. 40, 89–106.

Szabo, B.J., Kyser, T.K., 1990. Ages and stable isotope compositions of secondary calcite and opal in drill cores from Tertiary volcanic rocks of the Yucca Mountain area, Nevada. Geol. Soc. Am. Bull. 102, 1714–1719.

United States Department of Agriculture, 2007. Natural Resources Conservation Service. Soil survey of Pinnacles National Monument, California.

Vacco, D.A., Clark, P.U., Mix, A.C., Cheng, H., Edwards, R.L., 2005. A speleothem record of Younger Dryas cooling, Klamath Mountains, Oregon, USA. Quat. Res. 64, 249–256.

Vachon, R.W., Welker, J.M., White, J.W.C., Vaughn, B.H., 2010. Moisture source temperatures and precipitation δ^{18}O-temperature relationships across the United States. Water Resour. Res. 46.

Valley, J.W., Kita, N., 2009. In situ oxygen isotope geochemistry by ion microprobe. Mineralogical Society of Canada Short Course 41, Toronto, pp. 19–63 (May).

Wang, X.-L., Coble, M.A., Valley, J.W., Shu, X.-J., Kitajima, K., Spicuzza, M.J., Sun, T., 2014. Influence of radiation damage on late Jurassic zircon from southern China: Evidence from in situ measurement of oxygen isotopes, laser Raman, U-Pb ages, and trace elements. Chem. Geol. 389, 122–136.

Wolock, D.M., 2003. Hydrologic landscape regions of the United States. U.S. Geological Survey Open-File Report 03–145.

Wolock, D.M., Winter, T.C., McMahon, G., 2004. Delineation and evaluation of hydrologic-landscape regions in the United States using geographic information system tools and multivariate statistical analyses. Environ. Manag. 34, S71–S88.

Woo, K.S., Choi, D.W., Lee, K.C., 2008. Silicification of cave corals from some lava tube caves in the Jeju Island, Korea: implications for speleogenesis and a proxy for paleoenvironmental change during the Late Quaternary. Quat. Int. 176-177, 82–95.

Zhou, J., Lundstrom, C.C., Fouke, B., Panno, S., Hackley, K., Curry, B., 2005. Geochemistry of speleothem records from southern Illinois: Development of (^{234}U)/(^{238}U) as a proxy for paleoprecipitation. Chem. Geol. 221, 1–20.